The XRN1-regulated RNA helicase activity of YTHDC2 ensures mouse fertility independently of m^{6}A recognition

Li, Lingyun; Krasnykov, Kyrylo; Homolka, David; Gos, Pascal; Mendel, Mateusz; Fish, Richard; Pandey, Radha Raman; Pillai, Ramesh

How to cite

LI, Lingyun et al. The XRN1-regulated RNA helicase activity of YTHDC2 ensures mouse fertility independently of m^{6}A recognition. In: Molecular cell, 2022, vol. 82, n° 9, p. 1678–1690. doi: 10.1016/j.molcel.2022.02.034

This publication URL: https://archive-ouverte.unige.ch/unige:170029
Publication DOI: 10.1016/j.molcel.2022.02.034

Molecular Cell

Article

The XRN1-regulated RNA helicase activity of YTHDC2 ensures mouse fertility independently of m^{6}A recognition

Graphical abstract

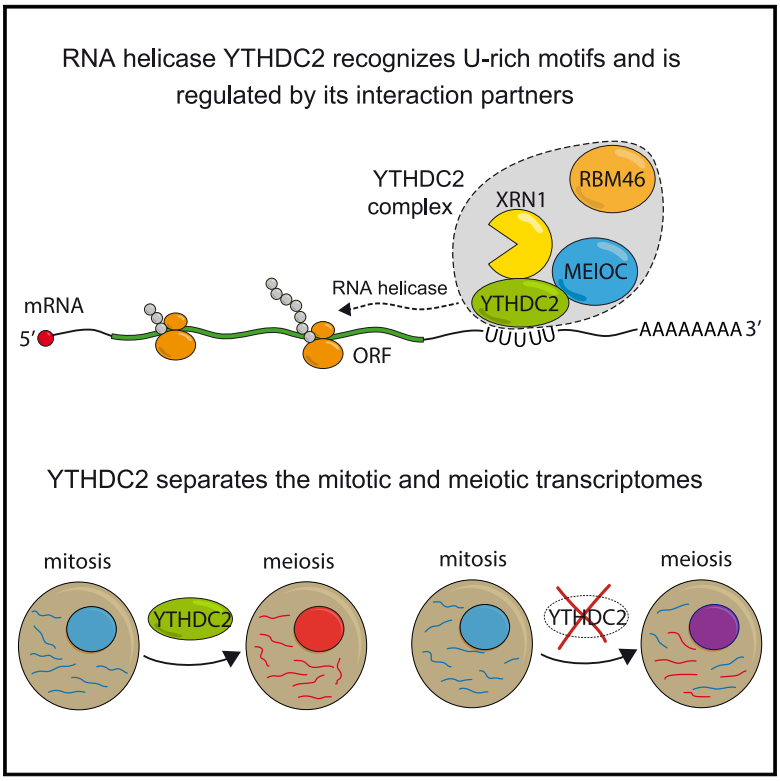

Highlights

- m^{6}A-reading capacity of YTHDC2 is not essential for mouse fertility
- YTHDC2 binds U-rich motifs in 3′ UTR of mRNAs
- The essential RNA helicase activity of YTHDC2 is enhanced by XRN1
- *Ythdc2* mutant germ cells have a mixed mitotic-meiotic identity

Authors

Lingyun Li, Kyrylo Krasnykov, David Homolka, ..., Richard J. Fish, Radha Raman Pandey, Ramesh S. Pillai

Correspondence

raman.pandey@unige.ch (R.R.P.), ramesh.pillai@unige.ch (R.S.P.)

In brief

Li et al. show that the m^{6}A-reading capacity of YTHDC2 is not essential for mouse fertility, but instead it binds U-rich motifs on RNAs and depends on its essential RNA helicase activity. YTHDC2 allows fine separation of the mitotic and meiotic transcriptomes as germ cells transition into meiosis.

Li et al., 2022, Molecular Cell *82*, 1678–1690
May 5, 2022
https://doi.org/10.1016/j.molcel.2022.02.034

CellPress

CellPress
OPEN ACCESS

Molecular Cell

Article

The XRN1-regulated RNA helicase activity of YTHDC2 ensures mouse fertility independently of m^{6}A recognition

Lingyun Li,[1,3] Kyrylo Krasnykov,[1,3] David Homolka,[1] Pascal Gos,[1] Mateusz Mendel,[1] Richard J. Fish,[2] Radha Raman Pandey,[1,*] and Ramesh S. Pillai[1,4,*]

[1]Department of Molecular Biology, Science III, University of Geneva, 30 Quai Ernest-Ansermet, CH-1211 Geneva 4, Switzerland
[2]Department of Genetic Medicine and Development, Faculty of Medicine, University of Geneva, 1 rue Michel-Servet, CH-1211 Geneva 4, Switzerland
[3]These authors contributed equally
[4]Lead contact
*Correspondence: raman.pandey@unige.ch (R.R.P.), ramesh.pillai@unige.ch (R.S.P.)
https://doi.org/10.1016/j.molcel.2022.02.034

SUMMARY

The functional consequence of N^6-methyladenosine (m^{6}A) RNA modification is mediated by "reader" proteins of the YTH family. YTH domain-containing 2 (YTHDC2) is essential for mammalian fertility, but its molecular function is poorly understood. Here, we identify U-rich motifs as binding sites of YTHDC2 on 3′ UTRs of mouse testicular RNA targets. Although its YTH domain is an m^{6}A-binder *in vitro*, the YTH point mutant mice are fertile. Significantly, the loss of its 3′→5′ RNA helicase activity causes mouse infertility, with the catalytic-dead mutation being dominant negative. Biochemical studies reveal that the weak helicase activity of YTHDC2 is enhanced by its interaction with the 5′→3′ exoribonuclease XRN1. Single-cell transcriptomics indicate that *Ythdc2* mutant mitotic germ cells transition into meiosis but accumulate a transcriptome with mixed mitotic/meiotic identity that fail to progress further into meiosis. Finally, our demonstration that *ythdc2* mutant zebrafish are infertile highlights its conserved role in animal germ cell development.

INTRODUCTION

RNAs are decorated with several chemical modifications, with N^6-methyladenosine (m^{6}A) being abundant on mRNAs (Fu et al., 2014; Roignant and Soller, 2017; Schwartz, 2016). The RNA methyltransferase "writer" complex composed of the METTL3-METTL14 heterodimer (Liu et al., 2014; Śledź and Jinek, 2016; Wang et al., 2016b) installs the modification on thousands of transcripts within the sequence context DR**A**CH (D = A, G or U; R = G or A; H = A, C or U; **A** = m^{6}A) (Dominissini et al., 2012; Meyer et al., 2012; Schwartz et al., 2013). Another writer, METTL16, catalyzes the mark on extended motifs (UAC**A**GAGAA or UAC**A**GAAAC) that are in the single-stranded region of a secondary structure on select RNAs (Doxtader et al., 2018; Mendel et al., 2018; Mendel et al., 2021; Pendleton et al., 2017; Ruszkowska et al., 2018; Warda et al., 2017). METTL3 (Batista et al., 2014; Geula et al., 2015) and METTL16 (Mendel et al., 2018) are essential for mouse embryonic development.

Presence of the m^{6}A methylation can have two major consequences: they can either repel proteins that would otherwise normally bind the unmethylated sequence or enable specific binding by "reader" proteins that can recognize the mark (Edupuganti et al., 2017). As an example of the former situation, 3′ splice site m^{6}A is shown to repel binding of the splicing factor U2AF35, inhibiting RNA splicing (Mendel et al., 2021; Watabe et al., 2021; Yoshida et al., 2020). However, much of the biology of m^{6}A is believed to be mediated by "reader" proteins, with the conserved YTH family of proteins being the best studied (Patil et al., 2018; Stoilov et al., 2002; Zhang et al., 2010). The signature YTH domain of these family members specifically recognizes m^{6}A within an aromatic pocket to bind RNAs (Li et al., 2014; Luo and Tong, 2014; Theler et al., 2014; Xu et al., 2014; Zhu et al., 2014). Subsequently, they recruit additional factors to alter splicing, RNA stability or translation. There are five mammalian members of the YTH family, with nuclear YTHDC1 being involved in regulating splicing, RNA stability, and alternative polyadenylation site choice (Kasowitz et al., 2018; Xiao et al., 2016). The YTHDF1, YTHDF2, and YTHDF3 are cytosolic and have redundant roles in regulating RNA stability or translation (Lasman et al., 2020; Wang et al., 2014; Wang et al., 2015; Zaccara and Jaffrey, 2020). The YTHDF proteins recruit the CCR4-NOT deadenylation complex to destabilize RNAs (Du et al., 2016; Liu et al., 2020; Wang et al., 2014). Consistent with their important roles, loss of mouse YTHDC1 (Kasowitz et al., 2018) and YTHDF2 (Ivanova et al., 2017; Lasman et al., 2020) causes embryonic lethality.

YTHDC2 is the largest member of the YTH family, is cytosolic, and expressed exclusively in the animal germline. Loss of *Ythdc2* results in male and female infertility in mice (Bailey et al., 2017; Hsu et al., 2017; Jain et al., 2018; Liu et al., 2021; Wojtas et al., 2017). Destabilization of RNA and modulation of translation are

CellPress
OPEN ACCESS

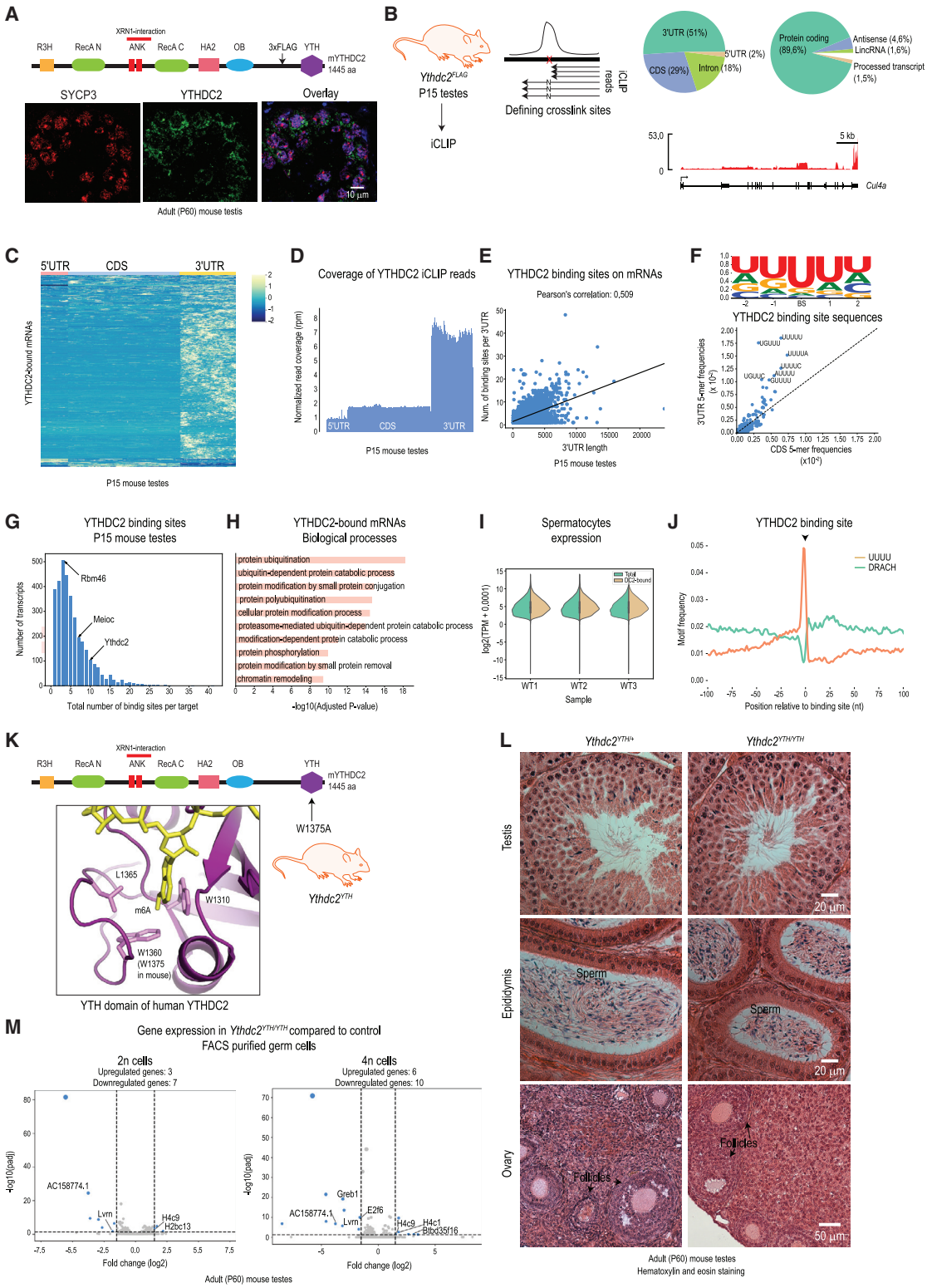

Figure 1. YTHDC2 binds to the 3′ UTR of protein-coding genes through a U-rich motif

(A) Cartoon showing domain organization of mouse YTHDC2 protein. The 3xFLAG tag sequence was inserted in the mouse *Ythdc2* gene locus between the OB-fold and the YTH domain. Immunofluorescence detection with anti-FLAG (green) and anti-SYCP3 (red) antibodies in adult (P60) testes sections of the *Ythdc2*^{FLAG} knockin mice. Scale bar in µm is indicated.

(legend continued on next page)

reported as consequences in the *Ythdc2* mutant germ cells, but precise mechanisms involved are unclear. YTHDC2 is a member of the DExH family of RNA helicases that is endowed with accessory RNA-binding domains like the R3H domain, oligo-nucleotide binding (OB) fold, and the YTH domain (Figure 1A). The YTH domain of YTHDC2 has the weakest RNA binding of all the YTH family members (Wojtas et al., 2017; Xu et al., 2015). For the same m^{6}A RNAs tested, binding affinities are at least 15- to 24-fold weaker for YTHDC2 when compared to YTHDC1 (Xu et al., 2015). This raises the question whether the specific m^{6}A-reading capacity of its YTH domain is relevant *in vivo*, especially given the presence of other RNA-binding domains. YTHDC2 possesses a 3′→5′ RNA helicase activity (Jain et al., 2018; Wojtas et al., 2017), but its physiological relevance is not known, since the fly ortholog Bgcn, which is also important for fertility, lacks residues consistent with such an activity (Bailey et al., 2017; Jain et al., 2018; Li et al., 2009; Ohlstein et al., 2000). Immunoprecipitated YTHDC2 complexes contain the 5′→3′ exoribonuclease XRN1 (Kretschmer et al., 2018; Wojtas et al., 2017) and a largely disordered protein called MEIOC (Abby et al., 2016; Soh et al., 2017; Wojtas et al., 2017). Whether these associations are direct, and how they impact the function of YTHDC2 is not known. Finally, it was shown that *Ythdc2* mutant germ cells transition from mitotic spermatogonia to enter meiosis, but do not stay on course to complete meiosis (Bailey et al., 2017; Hsu et al., 2017; Jain et al., 2018; Wojtas et al., 2017). It is unclear why germ cells fail to make a successful transition into meiosis in the absence of *Ythdc2*.

Here, we identify binding sites for YTHDC2 as U-rich motifs in the 3′ UTR of testicular RNAs and reveal that its m^{6}A-binding property is dispensable *in vivo* in mice. However, its RNA helicase activity is essential for mammalian fertility. Biochemical studies reveal that its helicase activity is restrained by structural inserts placed within the RNA helicase domain, but this design allows positive regulation by its interaction partner XRN1. Using single-cell transcriptomics, we identify a role for YTHDC2 in ensuring proper separation of transcriptomes when the germ cells transition from mitosis to meiosis, because mutant cells display a mixed transcriptome identity that is not conducive for proper meiotic progression. Finally, using a zebrafish knockout model, we demonstrate a conserved role for YTHDC2 in ensuring animal fertility.

RESULTS

YTHDC2 binds RNA targets with U-rich motifs

To understand the role of YTHDC2 in mouse testes, we wished to identify its RNA targets. Our previous attempts with a rabbit polyclonal antibody to purify YTHDC2-bound RNAs from mouse testes were unsuccessful. Therefore, we created a knockin mouse line expressing the 3x-FLAG-tagged fusion protein (STAR Methods). We inserted the tag at an internal location in a surface-accessible loop (defined by limited proteolysis of the recombinant YTHDC2 protein) between the OB fold and the YTH domain (Figures 1A and S1A). Such homozygous knockin *Ythdc2*^{FLAG} mice are viable and fertile.

The maximal expression of YTHDC2-FLAG protein was observed in the pachytene stage spermatocytes labeled with the meiotic marker SYCP3 (Figure 1A). To identify RNA targets of YHTDC2, we used testes from *Ythdc2*^{FLAG} animals at postnatal day 15 (P15), the developmental time-point when pachytene spermatocytes dominate the cell types present in the seminiferous tubules. Testicular cell suspensions were exposed to UV light, and the crosslinked YTHDC2-RNA complexes were isolated by anti-FLAG affinity beads (STAR Methods). After deep-sequencing of associated RNAs using the iCLIP protocol (Huppertz et al., 2014), the reads were mapped to the mouse genome (Figure S1B).

We defined the crosslink sites based on previously established criteria (Krakau et al., 2017). Briefly, a pile up of iCLIP

(B) Testes from *Ythdc2*^{FLAG} mice (P15) were used to perform iCLIP experiment to identify the YTHDC2-bound RNAs. Binding sites were identified as loci having a pile-up of reads with 3′ ends terminating at the potential crosslinking site or by reads crossing it but having an increased rate of indels. Pie charts showing proportion of YTHDC2 binding sites in different RNA biotypes, and the location of the YTHDC2 binding sites over different RNA features. The coverage of iCLIP reads over a representative target is shown. Notice the enrichment on the 3′ UTR.

(C) Heatmap showing z-scores of the iCLIP read coverage per binned YTHDC2-bound transcripts. See also Table S2.

(D) Metaplot showing an average iCLIP read coverage over YTHDC2 target transcripts.

(E) Scatterplot and the correlation analysis of the number of YTHDC2 binding sites against 3′ UTR length.

(F) Sequence logo showing a U-rich motif centered on the YTHDC2 binding site (BS) in a 5-mer window. Scatterplot comparing the 3′ UTRs and CDS frequency of all the pentamers centered on the YTHDC2 crosslink site (mostly a uridine). Top seven 5-mers found at the crosslink site are highlighted. See also Figure S1G.

(G) Histogram showing a distribution of the total number of binding sites per transcript.

(H) Gene ontology analysis of YTHDC2 targets. Only terms with the adjusted p value < 0.5 were plotted.

(I) Violin plots showing the distribution of expression counts (TPM + 0.0001) of all genes (green) in spermatocytes from P15 wild-type mouse testes, next to the distribution of expression counts (TPM + 0.0001) of YTHDC2 targets (orange). Three biological replicates are shown. Although transcripts bound by YTHDC2 have a broad expression profile, they show a slightly higher expression.

(J) Distribution of putative m^{6}A methylation sites (DRACH) and a U-rich sequence (UUUU) in a 200-nt window flanking the YTHDC2 binding site (position 0). See also Figures S1E and S1F.

(K) A modeled m^{6}A nucleotide in the hydrophobic pocket of the YTH domain of human YTHDC2 from (Wojtas et al., 2017). Key residues required for m^{6}A recognition are indicated. Mutation of W1360 is shown to abolish m^{6}A binding. The corresponding W1375 in the *Ythdc2*^{YTH} was mutated to assess physiological relevance of the YTH domain *in vivo*. See also Figure S1H.

(L) Eosin and hematoxylin-stained adult testis and ovary sections from heterozygous and homozygous *Ythdc2*^{YTH} knockin mutant mice. No difference was observed. Scale bar in μm is indicated.

(M) Ribo-depleted RNA-seq (in biological triplicates) analysis of FACS-purified 2n (spermatogonia) and 4n (spermatocytes) cells from mouse testes of heterozygous and homozygous *Ythdc2*^{YTH} knockin mutant mice. Volcano plots show the differential gene expression between the genotypes. Genes showing significant differential expression (padj < 0.05 and log2FC > 1.5 or log2FC < −1.5) are marked in blue. Significantly dysregulated pseudogenes are masked.

reads at a particular locus is considered to be a strong indicator of a binding site. The nucleotide that is crosslinked to the protein acts as a roadblock during reverse transcription, leading to termination of reads. In those cases where the reverse transcriptase traverses the crosslinked nucleotide, it introduces indels at the site (Figure 1B). These features were used to identify over ~34K YTHDC2 binding sites on thousands of testicular transcripts (Table S2). Most (90%) of these transcripts are protein-coding mRNAs, with majority (51%) of the binding sites being in the 3′ UTR of the RNAs (Figures 1B and S1D). When mapped to specific transcripts, a clear enrichment of the iCLIP reads on the 3′ UTR is visible (Figure 1B). A similar pattern emerges when reads are mapped to all YTHDC2-bound mRNAs (Figure 1C). A meta-plot of reads mapping to all the YTHDC2-bound protein-coding transcripts confirms this general trend for the protein to be mostly bound to the 3′ UTR, followed by some enrichment in the coding domain sequence (CDS) (Figure 1D). There is no strong correlation between the 3′ UTR length and the number of binding sites (Figure 1E). This enrichment is consistent with the known 3′→5′ RNA helicase activity of YTHDC2 (Jain et al., 2018; Wojtas et al., 2017), requiring a 3′ end loading on the RNA substrate.

Examination of the sequences at the crosslink site shows that a uridine is the preferred nucleotide, while the flanking nucleotides are also mostly uridines. Thus, as defined by this UV crosslinking approach, a U-rich motif defines the binding site of YTHDC2 (Figure 1F). We collected all 5-nt motifs centered on the crosslink site and examined their frequency of occurrence in the 3′ UTR and the coding domain sequence (CDS) (Figures 1F, S1E, and S1F). This analysis reveals two aspects of the YTHDC2 binding sites: first, several U-rich motifs (UUUUU, UGUUU, UGUUC, or AUUUU, etc.) dominate the crosslink site, with the allowance of additional nucleotides within it; second, these motifs are mostly present in the 3′ UTRs. Electrophoretic mobility shift assays (EMSA) with a radiolabelled RNA and recombinant human YTHDC2 confirms this preference for U-rich sequence to be directly determined by the protein itself (Figure S1G). Taken together, this suggests that YTHDC2 is loaded at the 3′ end of mRNAs using U-rich motifs as landing sites.

Transcripts from over 5000 genes are identified as bound by YTHDC2 in the P15 mouse testes (Table S2), with most transcripts having anywhere from 1 to 5 binding sites (Figure 1G). Interestingly, *Ythdc2* and its interaction partner *Meioc* are represented in this list (Figure 1G). A Gene Ontology (GO) analysis reveals a predominant presence of mRNAs associated with the ubiquitination pathway (Figure 1H), with ~500 transcripts belonging to this category (Table S2). The presence in the iCLIP dataset is not due to any aberrant high expression of these genes, as we find the YTHDC2-bound transcripts to have a broad expression pattern in the germ cells (Figure 1I). We propose that collective regulation of the few thousand transcripts that are bound by YTHDC2 in P15 testes is important for germ cell development.

m^{6}A-binding activity of YTHDC2 is dispensable for its function *in vivo*

YTHDC2 belongs to the YTH family of m^{6}A readers (Patil et al., 2018). The isolated YTH domain of YTHDC2 binds m^{6}A RNAs *in vitro*, albeit with binding affinities (K_d = 6-24 μM for YTHDC2) (Wojtas et al., 2017; Xu et al., 2015) that are at least 15-24 fold weaker than that for other YTH family members (K_d = 0.4-1 μM for YTHDC1) (Xu et al., 2015). This raises the question whether YTHDC2, which has several RNA-binding modules, depends on the YTH domain for its *in vivo* functions.

We first asked whether the U-rich motifs (YTHDC2 crosslink sites) identified on the testicular transcripts are near potential m^{6}A methylation sites (as defined by DRACH motifs). When examined in a 200-nt window flanking the crosslink site, we do not find any preference for having the DRACH motifs (Figure 1J). To directly test the *in vivo* relevance of the YTH domain, we edited the mouse genome to introduce a point mutation that was previously shown to abolish m^{6}A-specific RNA binding *in vitro* (Wojtas et al., 2017). This converts an aromatic tryptophan (W1375A) in the hydrophobic pocket of the YTH domain, to an alanine (Figures 1K and S1H). Heterozygous and homozygous *Ythdc2*^{YTH} knockin mice with the mutant YTH domain were found to be viable and fertile. These animals were maintained in our facility for over 2 years without any long-term defects in fertility. Histological examination of testes and ovaries from the homozygous *Ythdc2*^{YTH} knockin mice did not show any differences (Figure 1L). Mature sperm was identified in the epididymis of the homozygous mutant, while ovarian follicles at different stages of development were also observed (Figure 1L). Testicular transcriptome analysis of sorted 2n and 4n germ cells from adult (P60) mice also did not reveal any dramatic differences between the control heterozygous and homozygous *Ythdc2*^{YTH} knockin animals (Figure 1M). Taken together, we find that the ability to read m^{6}A modification is not essential for the *in vivo* roles of YTHDC2 in the mouse germline.

YTHDC2 directly associates with XRN1 and MEIOC but likely in separate complexes *in vivo*

Next, we focused on the YTHDC2-associated factors previously identified by immunoprecipitation experiments. This includes the 5′→3′ exoribonuclease XRN1 (Kretschmer et al., 2018; Wojtas et al., 2017) and a largely disordered protein with a coiled-coil domain called MEIOC (Figure 2A) (Abby et al., 2016; Soh et al., 2017). To determine if these associations are due to direct interactions, we expressed recombinant versions of the human proteins. YTHDC2 was produced as a full-length recombinant protein in the insect cell expression system, while the two others were produced as truncations: XRN1 (1-1279 aa) with a large deletion in the C-terminal disordered region, and the isolated conserved C-terminal coiled-coil (CC) domain of MEIOC (STAR Methods).

When co-expressed together, YTHDC2 and XRN1 (1-1279 aa) co-purify, and elute as a complex during size-exclusion chromatography (Figures 2A and S2A). Likewise, co-expressed YTHDC2 and the MEIOC-CC domain also co-purify together (Figure 2B). The two ankyrin (ANK) repeats of YTHDC2 are essential for interaction with XRN1 (Kretschmer et al., 2018; Wojtas et al., 2017). Deleting these repeats in the YTHDC2$^{\Delta ANK}$ protein did not affect its co-purification with MEIOC-CC domain (Figure 2B), indicating that YTHDC2 associates with its two partner proteins via distinct domains. Taken together, we demonstrate direct interactions between YTHDC2 and XRN1 (1-1279

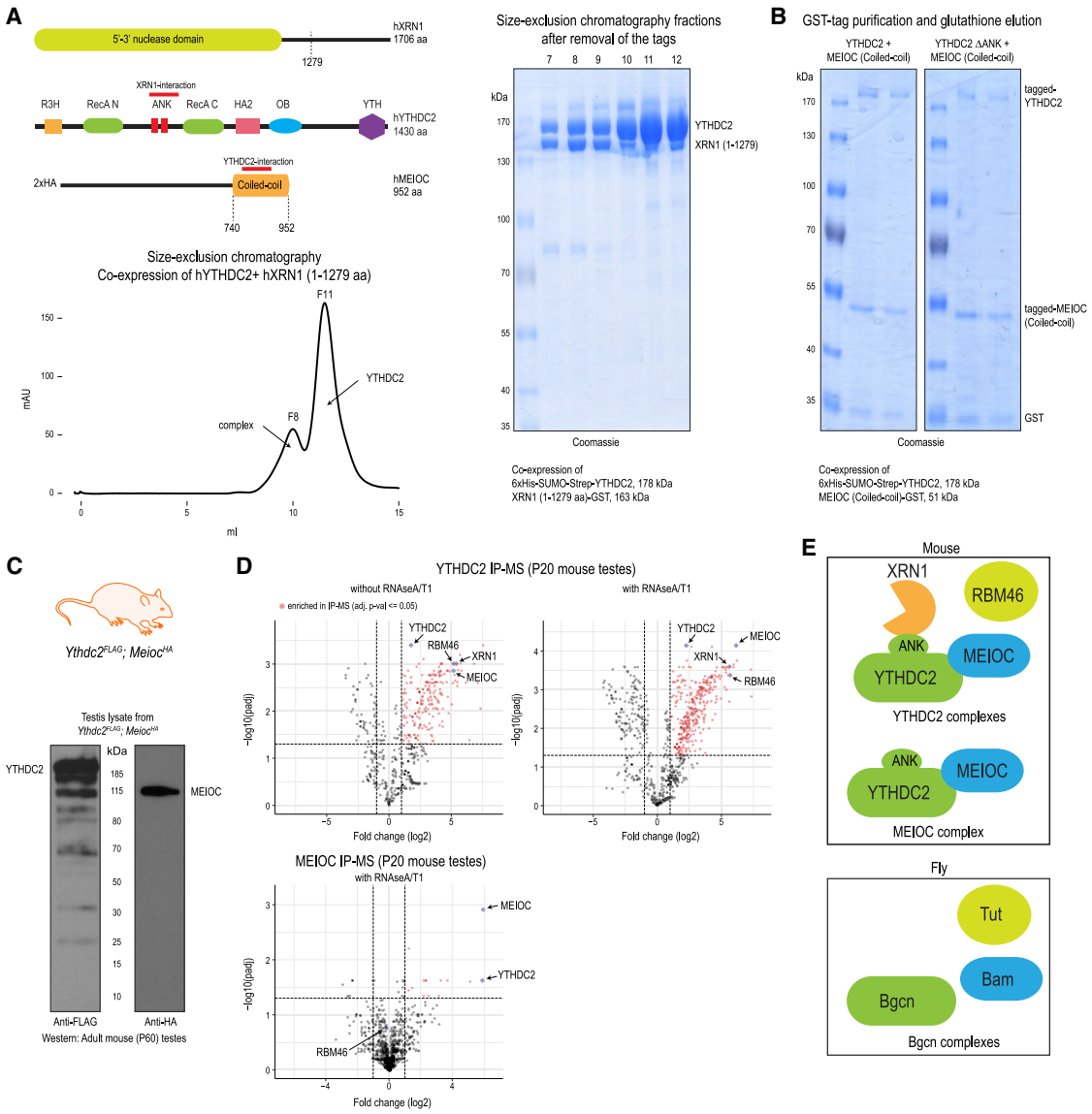

Figure 2. YTHDC2 directly interacts with XRN1 and MEIOC, and associates with RBM46

(A) Cartoon showing domain organization of human YTHDC2, XRN1 and MEIOC. The interaction regions in the proteins are marked. Size-exclusion chromatography protein elution trace showing the presence of YTHDC2-XRN1(1-1279 aa) complex and free YTHDC2 protein. Indicated fractions were analyzed by SDS-PAGE to reveal presence of YTHDC2- XRN1(1-1279 aa) complex (fractions 7-9) and free YTHDC2 (fractions 10–12). See also Figure S2A.

(B) Co-expression YTHDC2 and MEIOC-coiled-coil (CC) domain in insect cells as tagged proteins, followed by purification over glutathione-Sepharose beads to isolate MEIOC-CC. SDS-PAGE analysis shows the co-purification of YTHDC2 with MEIOC-CC (left panel). Deletion of the ANK repeats of YTHDC2 does not affect this association (right panel).

(C) Western blot of testicular lysate showing expression of YTHDC2-3xFLAG and 2xHA-MEIOC from double-knockin *Ythdc2*^{FLAG};*Meioc*^{HA} mice.

(D) Purification of protein complexes using anti-FLAG or anti-HA affinity beads. Complexes were treated with RNases (RNase A/T1), when indicated. Mass spectrometry identification of complex components is shown. The volcano plot shows the enrichment of proteins in purifications from knockin mouse testes lysates compared to that from wildtype mouse testes. See also Table S3.

(E) Cartoon showing the different protein associations of mouse YTHDC2 as established in this study in mouse testes. Complex components previously reported to be associating with YTHDC2 fly ortholog Bgcn is also shown.

aa), and between YTHDC2 and the coiled-coil (CC) domain of MEIOC.

To determine if the three proteins exist together *in vivo*, we generated *Meioc*^{HA} knockin mice expressing the HA-MEIOC tagged protein (Figure S2B) and crossed it with the *Ythdc2*^{FLAG} knockin mice. Such double knockin *Ythdc2*^{FLAG};*Meioc*^{HA} mice homozygous for both tagged alleles (Figure 2C) are viable and fertile, confirming that the tagged proteins were fully functional. We isolated endogenous complexes from P20 mouse testes using anti-FLAG or anti-HA affinity beads and subjected them to

mass spectrometry. YTHDC2-FLAG complexes enrich for both XRN1 and MEIOC (Figure 2D). Consistent with their direct interactions with YTHDC2 (Figures 2A and 2B), their presence in the endogenous complexes is resistant to treatment with RNases (Figure 2D). Interestingly, while HA-MEIOC complexes contained YTHDC2, we did not find XRN1 (Figures 2D, S2C, and S2D). This leads us to conclude that YTHDC2 exists in separate complexes with XRN1 and MEIOC *in vivo* (Figure 2E). While there are several other factors present, we report the presence of RNA binding motif protein 46 (RBM46) in the YTHDC2 purifications. Pointing to a role for RBM46 in animal fertility, zebrafish *rbm46* mutants reveal arrested meiosis and are infertile (Dai et al., 2021). Furthermore, the fly ortholog of RBM46 is the RNA recognition motif containing protein called Tumorous testis (Tut), also shown to be associated with Bgcn (Chen et al., 2014), the fly ortholog of YTHDC2. Taken together, we conclude that YTHDC2 forms specific sub-complexes *in vivo* in mouse testes and identify RBM46 as an additional component of the mouse YTHDC2 complex.

Ythdc2 RNA helicase catalytic-dead mutation is dominant-negative and blocks spermatogenesis

Having identified the RNA targets and protein complexes of YTHDC2, we next examined the relevance of its RNA helicase activity. RNA helicases utilize energy from ATP hydrolysis for unwinding RNA or displacing proteins or for mediating conformational changes of RNA-protein complexes (Bleichert and Baserga, 2007; Linder and Jankowsky, 2011). We created a mouse knockin mutant that has a point mutation in the ATP hydrolysis motif DEVH (DEVH → DQVH; E332Q) (Figure S3A). This mutation was shown to abolish the *in vitro* ATP hydrolysis and RNA unwinding activity of human YTHDC2 (Wojtas et al., 2017). Single-mouse embryo injections with the CRISPR construct (STAR Methods) resulted in viable heterozygous catalytic-dead (*Ythdc2*$^{+/cat\text{-}dead}$) founder mice of both sexes (Figure S3A). When crossed with wildtype mating partners, such heterozygous *Ythdc2*$^{+/cat\text{-}dead}$ catalytic-dead mutant mice did not produce any litters, indicating that the E332Q mutation is dominant negative. Some homozygous *Ythdc2*$^{cat\text{-}dead/cat\text{-}dead}$ founder mice were obtained and were also found to be infertile.

To examine the defect in spermatogenesis, we sequenced the testis transcriptomes from P14 catalytic-dead mutant and control wildtype animals. Analysis indicates that most of the gene expression changes are downregulation of transcripts in the catalytic-dead mutant (Figures 3A and S3B). Comparison with transcriptomes of purified germ cell populations present in wildtype mouse testes indicates that most of the downregulated genes are those normally highly expressed in meiotic spermatocytes (Figure 3B). This points to arrested spermatogenesis in the catalytic-dead mutant testes, with germ cells not making a proper progression through meiosis. Thus, the RNA helicase activity of YTHDC2 is essential for meiosis in the mouse male germline.

Ankyrin repeats constrain helicase activity of YTHDC2 but interaction with XRN1 enhances it

YTHDC2 is a member of the DExH family of processive RNA helicases that show RNA-dependent ATPase activity (Jankowsky and Fairman, 2007; Pyle, 2008). This drives its 3′→5′ RNA unwinding activity (Jain et al., 2018; Wojtas et al., 2017). The helicase domain of YTHDC2 is unusual in being interrupted by two ankyrin (ANK) repeats. The predicted (AlphaFold) (Jumper et al., 2021) core helicase domain of human YTHDC2 reveals how the repeats are hitched to the central β sheet of the C-terminal RecA module (Figure 3C). ANK repeats are protein-protein interaction domains (Mosavi et al., 2004), which in the case of YTHDC2 are required for interaction with XRN1 (Kretschmer et al., 2018; Wojtas et al., 2017).

To examine the relevance of the ANK repeats, we purified the YTHDC2$^{\Delta ANK}$ protein lacking the repeats (Figure 3D) and used it in a fluorescence-based RNA unwinding assay to compare its activity to that of the wildtype protein. The assay uses an RNA duplex with a single-stranded 3′ overhang as the substrate (Figure 3E), where a longer single-stranded RNA is annealed to two shorter complementary single-stranded RNAs: one fluorescently labeled with Cy3 and another with the quencher BHQ. Unwinding of the duplexes by YTHDC2 will separate the Cy3 away from the quencher, generating the fluorescence signal. When the reactions were primed by addition of ATP, we observed a low level of unwinding activity with the full-length YTHDC2 (Figures 3F and S3C). In comparison, the YTHDC2$^{\Delta ANK}$ protein presented strikingly robust activity. This suggests that presence of the two ANK repeats between the RecA modules constrains the RNA unwinding activity of YTHDC2 (Figure 3C).

Interaction partners are shown to modulate the ATPase/unwinding activities of RNA helicases (Bleichert and Baserga, 2007; Bono et al., 2006; Mathys et al., 2014). Therefore, we asked whether XRN1 or MEIOC can modulate the helicase activity of YTHDC2. We prepared a catalytic-dead (E178Q) version of XRN1 (1-1279) and used it in RNA unwinding reactions. Strikingly, in comparison to the YTHDC2 alone, presence of XRN1^{E178Q}(1-1279) enhanced the activity of YTHDC2 (Figures 3G, S3D, and S3E), and this was a dose-dependent effect (Figure S3F). As expected, XRN1 alone did not show any unwinding activity (Figures S3E and S3F). Consistent with the requirement of the ANK repeats for interaction, addition of XRN1^{E178Q}(1-1279) to the YTHDC2$^{\Delta ANK}$ protein did not alter its helicase activity (Figure 3H and S3H). This suggests that interaction of XRN1 to the ANK repeats may alter the conformation of the RecA domains (Figure 3C), such that they take up more readily a closed state that favors ATP hydrolysis and RNA unwinding (Linder and Jankowsky, 2011). Indeed, ATP hydrolysis assays showed a ~2-fold increase in activity of YTHDC2 in the presence of XRN1 (Figures 3I and S3I). The enhancement of the helicase activity by XRN1 is specific, as addition of the MEIOC-CC domain, whose interaction with YTHDC2 is not via the ANK repeats (Figure 2B), did not alter the RNA unwinding activity (Figures 3G, S3D, and S3G). We conclude that YTHDC2 has a weak helicase activity per se, but its structural design allows enhancement of this activity by its interaction partner XRN1.

Single-cell transcriptomics identifies a mixed transcriptome in the *Ythdc2* mutant germ cells

To examine the gene regulation consequences due to loss of *Ythdc2*, we conducted single-cell transcriptome analysis. Histological analyses have shown that mitotic spermatogonia (SG) in the *Ythdc2* KO testes differentiate by initiating the meiotic transcription program (Bailey et al., 2017; Hsu et al., 2017; Jain

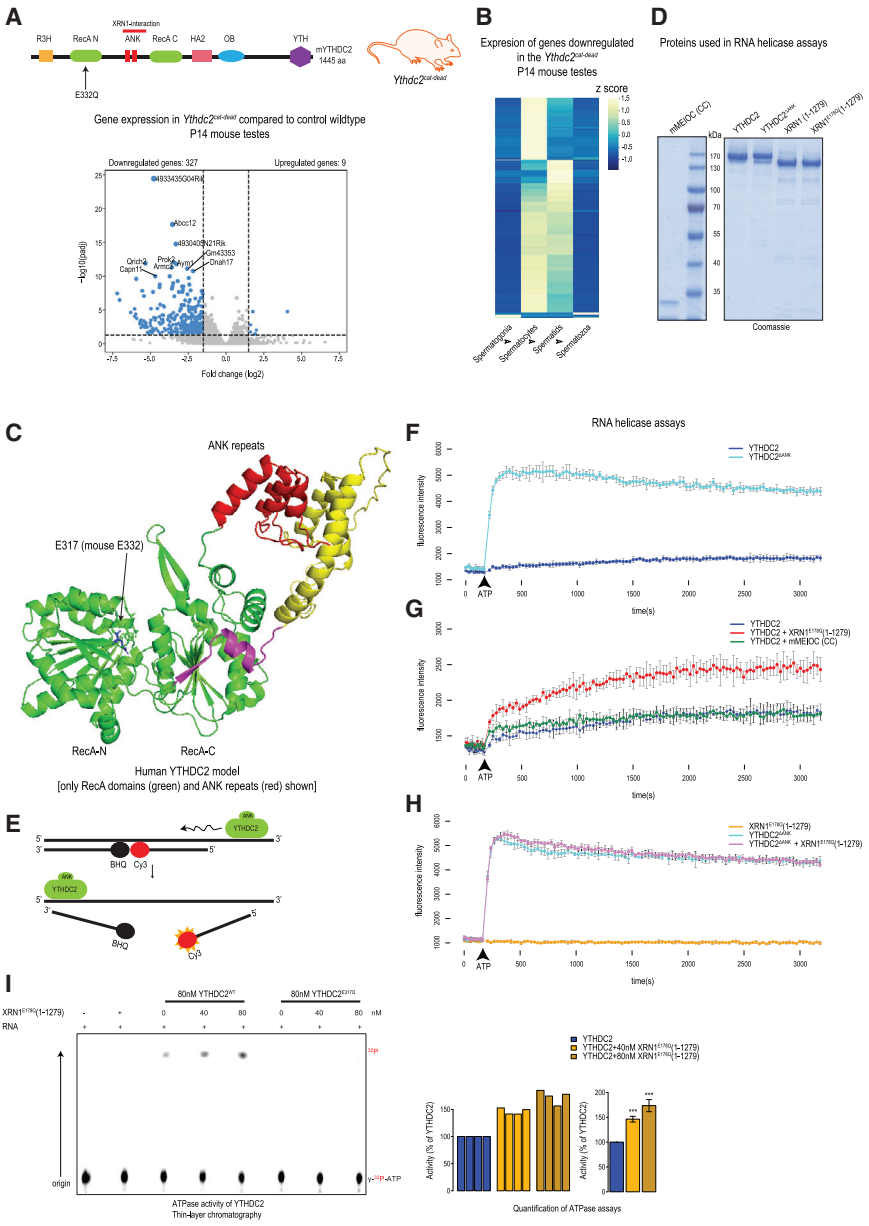

Figure 3. The essential 3′→5′ RNA helicase activity of YTHDC2 is modulated by XRN1

(A) Creation of the RNA helicase catalytic-dead *Ythdc2*$^{cat\text{-}dead}$ mouse mutant with the E332Q mutation in the N-terminal RecA domain. See also Figure S3A. Volcano plot showing differential testicular gene expression analysis between wildtype and *Ythdc2*$^{cat\text{-}dead}$ helicase mutant P14 mice. Significant genes (padj < 0.05 and log2FC > 1.5 or log2FC < −1.5) are shown in blue.

(B) Heatmap showing the expression pattern of significantly dysregulated genes (from the *Ythdc2*$^{cat\text{-}dead}$ mutant) in wildtype spermatogenic cell types. Z-scores from TPM counts are plotted. The genes downregulated in the mutant are those normally highly expressed in the spermatocytes and spermatids.

(C) Predicted (AlphaFold) structure of human YTHDC2, showing only the two RecA domains and the intervening two ankyrin (ANK) repeats. The helicase catalytic site glutamic acid (E) mutated in the *Ythdc2*$^{cat\text{-}dead}$ mouse mutant is indicated.

(D) Coomassie-stained gel (SDS-PAGE) of the recombinant human or mouse (m) proteins used for RNA unwinding assays.

(E) Schematic showing fluorescence-based RNA helicase assay. The Cy3 fluorescence is quenched in the duplex state. See also Table S1.

(F–I) (F) RNA helicase activity of full-length YTHDC2 and the ΔANK mutant. Deletion of ANK repeats enhances the helicase activity. Error bars refer to SD (G) RNA helicase activity of YTHDC2 in the presence of XRN1^{E178Q} (1-1279) or mouse MEIOC-CC domain. The addition of XRN1^{E178Q} (1-1279) enhances YTHDC2 helicase activity (red line). Error bars refer to SD (H) RNA helicase activity of the YTHDC2 ΔANK mutant is not affected by addition of XRN1^{E178Q} (1-1279). See also Figures S3E and S3F. Error bars refer to SD (I) thin-layer chromatography (TLC) analysis of ATP hydrolysis assays with full-length YTHDC2 or its catalytic-dead version. XRN1^{E178Q} (1-1279) was added in some of the reactions at the indicated concentrations. RNA is needed to stimulate the activity of YTHDC2. See also Figure S3I. Bar plots show the quantified YTHDC2 ATPase activity from four independent experiments. Addition of XRN1^{E178Q} (1-1279) enhances the ATPase activity of YTHDC2. Error bars refer to SD. The one tailed t test was used to test whether activity is higher than 100% (***p value < 0.001).

et al., 2018; Wojtas et al., 2017), but the mutant meiotic cells do not maintain this trajectory and undergo apoptosis. To examine more closely the cellular gene expression during this transition phase, we purified testicular germ cells from P10 animals that have replicated their DNA (4n) prior to entry into meiosis. Single-cell RNaseq libraries were prepared using the 10X Genomics technology (Figure 4A). We constructed single-cell maps based on the UMAP algorithm using expression data for 3000 highly variable genes (Figure 4B). Identity of the cell populations was established based on previous single-cell RNaseq of testicular cell types (Ernst et al., 2019).

The heterozygous *Ythdc2*$^{+/-}$ testes from P10 animals contained cells expected at this stage of spermatogenesis: undifferentiated spermatogonia (SG), differentiating SG, and meiotic leptotene/zygotene spermatocytes (L/Z SCs). While the knockout *Ythdc2*$^{-/-}$ testes had a similar set of cell types, it lacked the meiotic cells. Instead, two additional cell populations were present in the knockout testes (Figure 4B). Based on previous gene expression and histological analyses using the meiotic marker protein SYCP3 (Bailey et al., 2017; Hsu et al., 2017; Jain et al., 2018; Wojtas et al., 2017), *Ythdc2* mutant germ cells do make it into meiosis. Marker analyses reveal that the KO-specific cell populations have a mixed identity by having the transcriptomes present in both the differentiating SG and the meiotic cells (Figure 4C). They express several meiotic markers, including SYCP3 (Figure 4C), and markers normally expressed only in

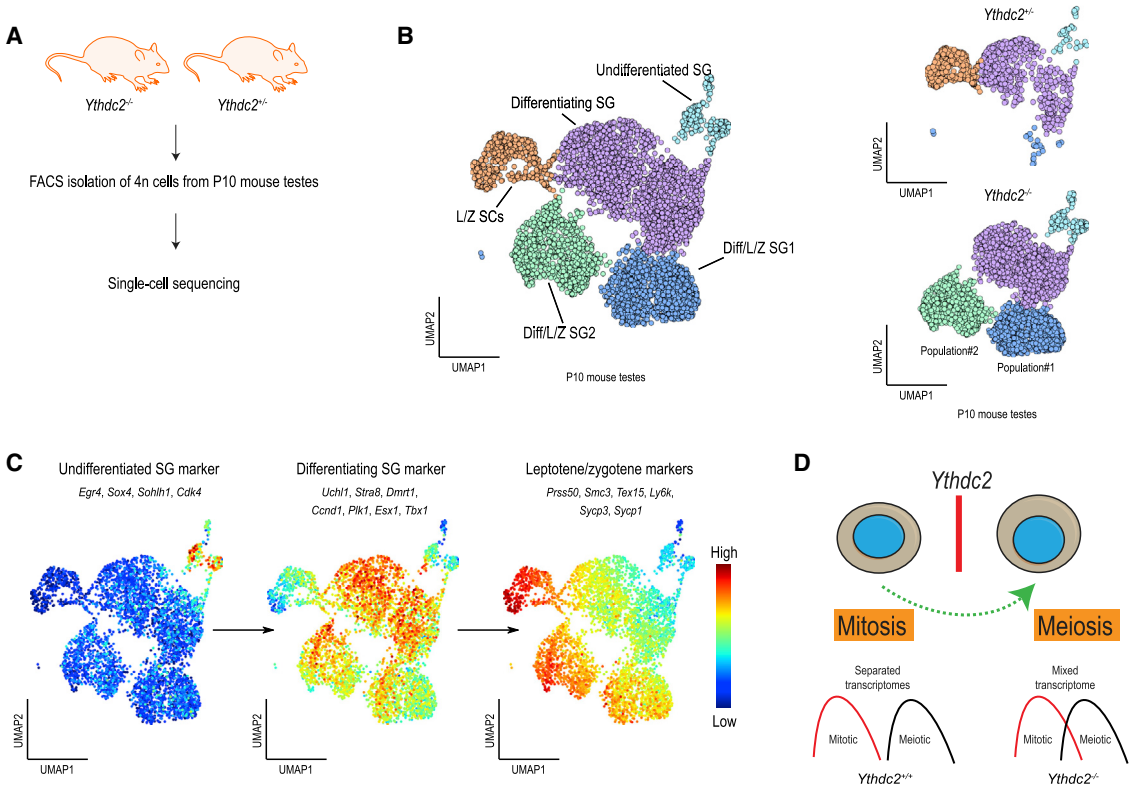

Figure 4. Loss of mouse *Ythdc2* results in germ cells with a mixed mitotic/meiotic identity

(A) Single-cell purification of 4n germ cells from mouse testes of *Ythdc2*$^{+/-}$ and *Ythdc2*$^{-/-}$ (KO) P10 animals.

(B) UMAP-based integrated single-cell map of *Ythdc2*$^{+/-}$ and *Ythdc2*$^{-/-}$ (KO) testicular 4n germ cells (left). Annotated cell types are assigned a specific color. Genotype-separated single-cell maps are shown (right). Notice the presence of two unique cell populations present only in the KO testes.

(C) Analysis of the indicated mitotic and meiotic marker genes expression. UMAP-based single-cell maps are ordered based on the developmental trajectory: mitotic spermatogonia (SG) marker expression (left), differentiating SG cell marker expression (middle), and leptotene/zygotene meiotic markers expression (right). Note that differentiating SG and meiotic markers are simultaneously expressed in the two populations of cells found exclusively in the *Ythdc2* KO. See also Figures S4B and S4C.

(D) Model showing how YTHDC2 acts during the mitotic-meiotic transition. In the absence of *Ythdc2*, germ cells display a mixed identity with expression of markers present in both differentiating SG and meiotic cells.

differentiating SG (Figure 4C). Interestingly, immunofluorescence analysis of *Meioc* KO germ cells reveals a simultaneous expression of the meiotic marker SYCP3 and the mitotic marker cyclin A2 (CCNA2) (Soh et al., 2017). Similarly, we find the expression of *Ccna2* in the two mixed-identity cell populations in the *Ythdc2* KO testes (Figure S4C). Taken together, our data show that YTHDC2 is required for a fine separation of the transcriptomes when germ cells make the transition from mitosis to meiosis (Figure 4D). In the absence of YTHDC2, cells transition into meiosis but still express mitotic genes, and such a mixed transcriptome fails to support further progression into meiosis.

ythdc2 has a conserved role in ensuring fertility in the zebrafish germline

To explore the conserved role of YTHDC2, we generated *ythdc2* mutant zebrafish (STAR Methods). The mutant allele has a 46-base-pair deletion (*ythdc2*$^{\Delta 46}$) in the region encoding the N-terminal RecA module of the RNA helicase domain (Figure S5A). Heterozygous (*ythdc2*$^{\Delta 46/+}$) adult fish are viable and fertile. When in-crossed, the heterozygous (*ythdc2*$^{\Delta 46/+}$) animals give rise to embryos (examined at 1 and 5 days post-fertilization; dpf) in the expected Mendelian ratios (Figure 5A). Interestingly, all the homozygous adult *ythdc2*$^{\Delta 46/\Delta 46}$ individuals we identified are phenotypically males, and none were phenotypically female. This distinction is made on the basis of a flatter body plan and reddish color of males compared to females. We note that masculinization of the homozygous individuals is also reported for the *rbm46* zebrafish mutants (Dai et al., 2021). The homozygous *ythdc2*$^{\Delta 46/\Delta 46}$ males are infertile, as crosses with wildtype females failed to produce any viable, fertilized embryos (Figure 5B). To study the spermatogenic defect, we examined the gonads in 6-month-old wild-type, heterozygous, and homozygous mutant adult males using standard histological staining. The wildtype and heterozygous gonads revealed multiple seminiferous tubules full of spermatozoa, surrounded by spermatogonia and spermatocytes at different stages and associated cell types, as expected. Somatic Leydig and Sertoli cells are hardly visible (Figures 5C, S5B, and S5C). Strikingly, the homozygous *ythdc2*$^{\Delta 46/\Delta 46}$ gonads are hollowed out with empty tubules lacking any trace of meiotic germ cells. An interstitium

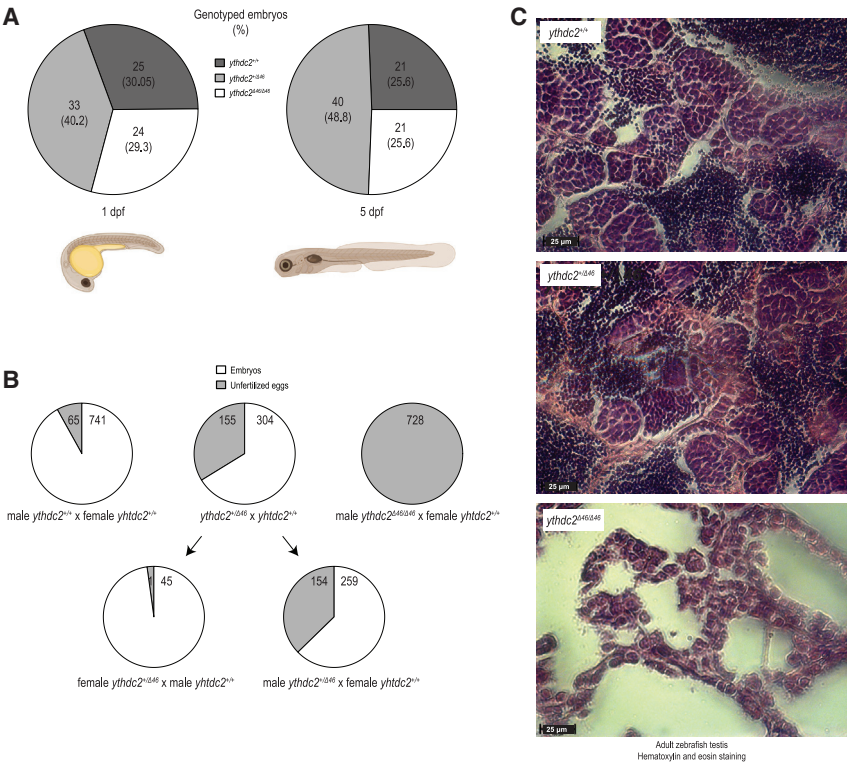

Figure 5. Conserved role of zebrafish *ythdc2* in male fertility

(A) Generation of *ythdc2* knockout (Δ46) zebrafish. Heterozygous crosses give rise to animals in the expected Mendelian ratios.

(B) Crosses of heterozygous and homozygous $ythdc2^{\Delta 46/\Delta 46}$ knockout males or females with wild-type partners. Crosses with homozygous knockout males do not produce any embryos, indicating that they are infertile. See also Figure S5B.

(C) Hematoxylin and Eosin staining of adult zebrafish testes showing that the infertile homozygous $ythdc2^{\Delta 46/\Delta 46}$ fish lack sperm. Scale bar in µm is indicated.

remains, but there are no cells corresponding to the germline. Taken together, this analysis confirms a conserved role for YTHDC2 in germline development from insects (Chen et al., 2014; Li et al., 2009) to zebrafish (Figure 5) and mice (Bailey et al., 2017; Hsu et al., 2017; Jain et al., 2018; Liu et al., 2021; Wojtas et al., 2017).

DISCUSSION

We (Wojtas et al., 2017) and others (Bailey et al., 2017; Hsu et al., 2017; Jain et al., 2018) previously demonstrated that YTHDC2 regulates m^{6}A transcripts in the mammalian germline. This hinged on the following observations. First, the isolated YTH domain of YTHDC2 has m^{6}A-reading activity *in vitro* and has a structural similarity to the m^{6}A-binding pocket of other YTH proteins (Hsu et al., 2017; Jain et al., 2018; Wojtas et al., 2017; Xu et al., 2015), although the binding is weaker compared to the domain found in other YTH proteins (Xu et al., 2015). Second, m^{6}A-enriched transcripts are enriched in YTHDC2 complexes (Bailey et al., 2017; Hsu et al., 2017). Third, the levels of these YTHDC2-bound RNA targets are increased in the absence of *Ythdc2* (Hsu et al., 2017) or levels of m^{6}A-enriched RNAs are increased in the *Ythdc2* mutant (Wojtas et al., 2017). Together, these suggested a role for YTHDC2 in post-transcriptional regulation by regulating RNA abundance or translation (Bailey et al., 2017; Hsu et al., 2017; Jain et al., 2018; Wojtas et al., 2017).

In this study, we examined the *in vivo* relevance of its m^{6}A-reading activity. This question is especially relevant for a protein like YTHDC2, as it is decorated with multiple RNA-binding domains (R3H domain, RNA helicase module, and the OB fold). We created mice with a single-amino-acid mutation in the YTH domain that is shown to abolish the m^{6}A-binding *in vitro* (Wojtas et al., 2017). Such mutant mice did not reveal any impact on fertility (Figure 1L). Therefore, we conclude that despite the isolated YTH domain having an affinity for m^{6}A RNAs *in vitro* (Hsu et al., 2017; Wojtas et al., 2017; Xu et al., 2015), YTHDC2 may not depend on its m^{6}A-reading activity for RNA binding *in vivo* (Figure 1). Instead, our iCLIP experiments identify U-rich motifs in the 3′ end of the RNAs as the binding sites for YTHDC2 (Figure 1F), with no enrichment of m^{6}A methylation motifs in its vicinity (Figure 1J). The previously made correlations between m^{6}A methylation and YTHDC2-association and RNA regulation, needed a sound genetic test of *in vivo* relevance, which we now provide. In the light of this result, we propose that m^{6}A recognition via the YTH domain is not the dominant force for RNA-binding by YTHDC2 *in vivo*. Instead, multivalent interactions via the other RNA binding domains (R3H, helicase domain and OB fold) provide this RNA-recognition ability. We find that recombinant human YTHDC2 on its own prefers to bind an oligo-U RNA sequence over an oligo-A RNA (Figure S1G). Structural studies of the DExH RNA helicase MLE shows how base-specific interaction with the OB fold can specify the binding to U-rich sequences (Prabu et al., 2015). Furthermore, the R3H domain is a single-stranded nucleic acid binding domain (Grishin, 1998), which in the polyA-specific ribonuclease (PARN) contributes to RNA binding but does not specify the target (Wu et al., 2005). In conclusion, we propose that in identifying its RNA targets, YTHDC2 prioritizes sequence-specific RNA binding over recognition of RNA modifications. This is reminiscent of the extreme case of the fission yeast YTH protein Mmi1 (Harigaya et al., 2006), where the YTH domain lacks the ability to recognize m^{6}A (Wang et al., 2016a), but instead uses a distinct structural feature in the domain for high-affinity binding to hexanucleotide motifs present in its RNA targets (Hiriart et al., 2012; Yamashita et al., 2012).

Once on the 3′ UTR (Figures 1C and 1D), YTHDC2 depends on its RNA helicase activity for its *in vivo* functions in the mouse

germline (Figure 3). Precisely what it achieves is currently not known. It probably translocates along the RNA in a 3′→5′ direction to unwind RNA structures or evict bound protein factors. It is also possible that it remodels RNA-protein complexes bound at the 3′ end of the RNA. Given that the ATPase (Figure 3I) and helicase activities (Figures 3F–3H) of YTHDC2 are regulated by the 5′→3′ exoribonuclease XRN1, this interaction likely provides a mechanism to tie the enhancement of RNA helicase activity to consequences like RNA degradation. Interestingly, the C-terminal low-complexity region of XRN1 is shown to directly associate with decapping and deadenylation factors, bridging enzymatic activities that act at both ends of the mRNA to promote mRNA decay (Chang et al., 2019). While we did not precisely map the domain on XRN1 for association with YTHDC2, this C-terminal low-complexity region is a good candidate to mediate it (Figure 2A). Furthermore, the precise contributions of MEIOC and RBM46 to the function of YTHDC2 is not clear. MEIOC interacts with its conserved coiled-coil (CC) domain to a region of YTHDC2 that is distinct from that used by XRN1, and this does not modulate the RNA helicase activity (Figure 3G).

YTHDC2 likely regulates thousands of RNA targets in the mouse germline. It directly binds ~5,000 transcripts (Table S2) via U-rich motifs (Figure 1F) in the P15 mouse testes, where pachytene spermatocytes are the dominant cell type in the seminiferous tubules. Transcripts acting in the ubiquitination pathway form a large class of the YTHDC2 targets (Table S2 and Figure 1H). While it is known that the ubiquitination pathway plays an essential role in removal of specific transcription factors or histones at defined steps during mouse spermatogenesis (Nakagawa et al., 2017), how regulation of this pathway by YTHDC2 contributes to progression through meiosis remains to be understood. Pointing to its relevance beyond the early mitosis-meiosis transition stage, conditional deletion of *Ythdc2* in the pachytene spermatocytes causes abrogation of germ cell development, leading to infertility (Liu et al., 2021).

Examination of single-cell transcriptomes of germ cells in the P10 mouse testes shows that YTHDC2 plays a critical role in enabling a fine separation of the transcriptomes as mitotic differentiating spermatogonia enter meiosis (Figure 4). In the absence of *Ythdc2*, mutant germ cells initiate meiosis, but accumulate a mixed transcriptome with mitotic/meiotic identity (Figures 4B and 4D). Such mutant germ cells fail to progress further in meiosis and undergo apoptosis (Bailey et al., 2017; Hsu et al., 2017; Jain et al., 2018; Wojtas et al., 2017). We favor a model where YTHDC2 regulates the decay of mitotic RNA targets during this mitosis-meiosis transition stage. We see an enrichment of U-rich motifs in the transcriptomes represented in the undifferentiated and differentiating spermatogonia, and in one of the mixed-identity *Ythdc2* KO-specific cell populations (Figure S4D). There is also an enrichment of ubiquitination pathway genes in these cell types when compared to the meiotic cells (Figure S4E). In contrast, the spermatocyte transcriptomes in the control P10 mouse testes are depleted of such U-rich motifs (Figure S4D). While the U-rich motifs may be one of the specificity elements in the YTHDC2 targets, other YTHDC2 complex components (like RBM46) may contribute to RNA target identification. YTHDC2 is now shown to be essential for germ cell development in the insect (Li et al., 2009), fish (Figure 5) and mouse (Bailey et al., 2017; Hsu et al., 2017; Jain et al., 2018; Liu et al., 2021; Wojtas et al., 2017) systems. Beyond this conservation of the role in fertility, at the molecular level the protein seems to use distinct mechanisms. The insect ortholog Bgcn lacks the YTH domain and amino acid residues consistent with ATPase and helicase activities (Jain et al., 2018; Ohlstein et al., 2000), but forms a complex with Bam and Tut (Chen et al., 2014), orthologs of mouse MEIOC and RBM46. Understanding this catalytic and non-catalytic contributions of YTHDC2 proteins to gene regulation will be an exciting question for the future.

Limitations of study

Although we show that the YTH domain of YTHDC2 is dispensable in the mouse germline, maintenance of this m^6A-reading capacity might indicate that it may be used in other contexts that are not examined in this study. YTHDC2 facilitates translation of *Hif1a* mRNA in mouse adipocytes under conditions of increased m^6A levels on the RNA (when the demethylase FTO is deleted), promoting white-to-beige fat transition (Wu et al., 2021). Another study reported that YTHDC2 is recruited by the m^6A-modified internal ribosome entry sites (IRES) of the hepatitis C virus (HCV) to promote cap-independent translation (Kim and Siddiqui, 2021). Furthermore, YTHDC2 is shown to facilitate translation of mRNAs with coding-region m^6A (Mao et al., 2019). Therefore, ruling out any role for the m^6A-reading activity of YTHDC2, especially outside the germline, maybe premature. We identified RNAs encoded by ~5,000 genes as YTHDC2 targets (Table S2), but how their collective regulation contributes to a successful mitotic-meiotic transition remains to be identified. It is also not clear if further specificity elements beyond U-rich motifs exist to define such targets. Contributions of YTHDC2-associated factors like MEIOC and RBM46 to its function need to be elucidated. One challenge we faced is in obtaining full-length MEIOC protein, even when co-expressed together with YTHDC2. This may indicate that additional factors are missing in the complex nucleated by YTHDC2, and our mass spectrometry data (Table S3) will facilitate further studies in this direction. Finally, the precise molecular mechanism by which YTHDC2 regulates its RNA targets remains to be discovered.

STAR★METHODS

Detailed methods are provided in the online version of this paper and include the following:

- KEY RESOURCES TABLE
- RESOURCE AVAILABILITY
  - Lead contact
  - Materials availability
  - Data and code availability
- EXPERIMENTAL MODEL AND SUBJECT DETAILS
  - Animal work
  - Genotyping PCR for $Ythdc2^{FLAG}$ mouse line
- METHOD DETAILS
  - Clones and constructs
  - Baculovirus-mediated insect cell protein expression
  - Purification of recombinant proteins and complexes
  - YTHDC2 RNA helicase assay

- ATPase assay
- Electrophoretic Mobility Shift Assay (EMSA)
- Antibodies
- Isolation of endogenous YTHDC2 and MEIOC complexes from mouse testes
- Tissue lysates
- Western Blot
- Histology and Immunofluorescence
- FACS purification of mouse germ cells for RNaseq and single-cell RNA sequencing
- Preparation of RNA libraries

- QUANTIFICATION AND STATISTICAL ANALYSIS
  - iCLIP
  - Analysis of RNA-seq data
  - Analysis of single cell sequencing data

SUPPLEMENTAL INFORMATION

Supplemental information can be found online at https://doi.org/10.1016/j.molcel.2022.02.034.

ACKNOWLEDGMENTS

We thank Prof. Bart Deplancke for advice on single-cell transcriptome analysis, and Nicolas Roggli for scientific illustrations. Help from the following core facilities at University of Geneva is acknowledged: Transgenic mouse facility, Zebrafish Core Facility, iGE3 Genomics Platform, Histology, and Bioimaging Center. We also thank the Genomics Core at EMBL Heidelberg, the Functional Genomics Center, Zurich for proteomics analyses. L.L. is supported by an iGE3 PhD Fellowship. This work was supported by grants to R.S.P. from the Swiss National Science Foundation, Switzerland (ERC Transfer Grant CRETP3_166923, Project Grant 310030B_185386, and Sinergia Grant CRSII5_183524, and funding from the NCCR RNA & Disease 51NF40_182880). Work in the Pillai lab is supported by the Republic and Canton of Geneva.

AUTHOR CONTRIBUTIONS

L.L. purified recombinant proteins and performed biochemical assays; K.K. performed analysis of deep sequencing datasets; P.G. prepared FACS-purified germ cells; D.H. performed analysis of mass spectrometry data and assembled all the figures; M.M. and R.J.F. prepared and analyzed the zebrafish mutant; R.R.P. created mouse mutants, generated deep sequencing libraries from mouse samples, performed iCLIP and designed the study together with R.S.P.; manuscript preparation and writing by R.S.P. with input from everyone.

DECLARATION OF INTERESTS

The authors declare no competing interests.

Received: November 21, 2021
Revised: February 22, 2022
Accepted: February 23, 2022
Published: March 18, 2022

REFERENCES

Abby, E., Tourpin, S., Ribeiro, J., Daniel, K., Messiaen, S., Moison, D., Guerquin, J., Gaillard, J.C., Armengaud, J., Langa, F., et al. (2016). Implementation of meiosis prophase I programme requires a conserved retinoid-independent stabilizer of meiotic transcripts. Nat. Commun. *7*, 10324.

Altschul, S.F., Madden, T.L., Schäffer, A.A., Zhang, J., Zhang, Z., Miller, W., and Lipman, D.J. (1997). Gapped BLAST and PSI-BLAST: a new generation of protein database search programs. Nucleic Acids Res. *25*, 3389–3402.

Bailey, A.S., Batista, P.J., Gold, R.S., Chen, Y.G., de Rooij, D.G., Chang, H.Y., and Fuller, M.T. (2017). The conserved RNA helicase YTHDC2 regulates the transition from proliferation to differentiation in the germline. eLife *6*, e26116.

Bassett, A., and Liu, J.L. (2014). CRISPR/Cas9 mediated genome engineering in Drosophila. Methods *69*, 128–136.

Batista, P.J., Molinie, B., Wang, J., Qu, K., Zhang, J., Li, L., Bouley, D.M., Lujan, E., Haddad, B., Daneshvar, K., et al. (2014). m(6)A RNA modification controls cell fate transition in mammalian embryonic stem cells. Cell Stem Cell *15*, 707–719.

Bieniossek, C., Imasaki, T., Takagi, Y., and Berger, I. (2012). MultiBac: expanding the research toolbox for multiprotein complexes. Trends Biochem. Sci. *37*, 49–57.

Bleichert, F., and Baserga, S.J. (2007). The long unwinding road of RNA helicases. Mol. Cell *27*, 339–352.

Bono, F., Ebert, J., Lorentzen, E., and Conti, E. (2006). The crystal structure of the exon junction complex reveals how it maintains a stable grip on mRNA. Cell *126*, 713–725.

Bray, N.L., Pimentel, H., Melsted, P., and Pachter, L. (2016). Near-optimal probabilistic RNA-seq quantification. Nat. Biotechnol. *34*, 525–527.

Busch, A., Brüggemann, M., Ebersberger, S., and Zarnack, K. (2020). iCLIP data analysis: A complete pipeline from sequencing reads to RBP binding sites. Methods *178*, 49–62.

Chang, C.-T., Muthukumar, S., Weber, R., Levdansky, Y., Chen, Y., Bhandari, D., Igreja, C., Wohlbold, L., Valkov, E., and Izaurralde, E. (2019). A low-complexity region in human XRN1 directly recruits deadenylation and decapping factors in 5′-3′ messenger RNA decay. Nucleic Acids Res. *47*, 9282–9295.

Chen, E.Y., Tan, C.M., Kou, Y., Duan, Q., Wang, Z., Meirelles, G.V., Clark, N.R., and Ma'ayan, A. (2013). Enrichr: interactive and collaborative HTML5 gene list enrichment analysis tool. BMC Bioinformatics *14*, 128.

Chen, D., Wu, C., Zhao, S., Geng, Q., Gao, Y., Li, X., Zhang, Y., and Wang, Z. (2014). Three RNA binding proteins form a complex to promote differentiation of germline stem cell lineage in Drosophila. PLoS Genet. *10*, e1004797.

Dai, X., Cheng, X., Huang, J., Gao, Y., Wang, D., Feng, Z., Zhai, G., Lou, Q., He, J., Wang, Z., and Yin, Z. (2021). Rbm46, a novel germ cell-specific factor, modulates meiotic progression and spermatogenesis. Biol. Reprod. *104*, 1139–1153.

Dobin, A., Davis, C.A., Schlesinger, F., Drenkow, J., Zaleski, C., Jha, S., Batut, P., Chaisson, M., and Gingeras, T.R. (2013). STAR: ultrafast universal RNA-seq aligner. Bioinformatics *29*, 15–21.

Dominissini, D., Moshitch-Moshkovitz, S., Schwartz, S., Salmon-Divon, M., Ungar, L., Osenberg, S., Cesarkas, K., Jacob-Hirsch, J., Amariglio, N., Kupiec, M., et al. (2012). Topology of the human and mouse m6A RNA methylomes revealed by m6A-seq. Nature *485*, 201–206.

Doxtader, K.A., Wang, P., Scarborough, A.M., Seo, D., Conrad, N.K., and Nam, Y. (2018). Structural Basis for Regulation of METTL16, an S-Adenosylmethionine Homeostasis Factor. Mol. Cell *71*, 1001–1011.e4.

Du, H., Zhao, Y., He, J., Zhang, Y., Xi, H., Liu, M., Ma, J., and Wu, L. (2016). YTHDF2 destabilizes m(6)A-containing RNA through direct recruitment of the CCR4-NOT deadenylase complex. Nat. Commun. *7*, 12626.

Edupuganti, R.R., Geiger, S., Lindeboom, R.G.H., Shi, H., Hsu, P.J., Lu, Z., Wang, S.-Y., Baltissen, M.P.A., Jansen, P.W.T.C., Rossa, M., et al. (2017). N^6-methyladenosine (m^6A) recruits and repels proteins to regulate mRNA homeostasis. Nat. Struct. Mol. Biol. *24*, 870–878.

Ernst, C., Eling, N., Martinez-Jimenez, C.P., Marioni, J.C., and Odom, D.T. (2019). Staged developmental mapping and X chromosome transcriptional dynamics during mouse spermatogenesis. Nat. Commun. *10*, 1251.

Finak, G., McDavid, A., Yajima, M., Deng, J., Gersuk, V., Shalek, A.K., Slichter, C.K., Miller, H.W., McElrath, M.J., Prlic, M., et al. (2015). MAST: a flexible statistical framework for assessing transcriptional changes and characterizing heterogeneity in single-cell RNA sequencing data. Genome Biology *16*, 278.

Fish, R.J., Freire, C., Di Sanza, C., and Neerman-Arbez, M. (2021). Venous Thrombosis and Thrombocyte Activity in Zebrafish Models of Quantitative and Qualitative Fibrinogen Disorders. Int. J. Mol. Sci. *22*, 655.

Fu, Y., Dominissini, D., Rechavi, G., and He, C. (2014). Gene expression regulation mediated through reversible m^{6}A RNA methylation. Nat. Rev. Genet. *15*, 293–306.

Geula, S., Moshitch-Moshkovitz, S., Dominissini, D., Mansour, A.A., Kol, N., Salmon-Divon, M., Hershkovitz, V., Peer, E., Mor, N., Manor, Y.S., et al. (2015). Stem cells. m6A mRNA methylation facilitates resolution of naïve pluripotency toward differentiation. Science *347*, 1002–1006.

Grishin, N.V. (1998). The R3H motif: a domain that binds single-stranded nucleic acids. Trends Biochem. Sci. *23*, 329–330.

Harigaya, Y., Tanaka, H., Yamanaka, S., Tanaka, K., Watanabe, Y., Tsutsumi, C., Chikashige, Y., Hiraoka, Y., Yamashita, A., and Yamamoto, M. (2006). Selective elimination of messenger RNA prevents an incidence of untimely meiosis. Nature *442*, 45–50.

Hiriart, E., Vavasseur, A., Touat-Todeschini, L., Yamashita, A., Gilquin, B., Lambert, E., Perot, J., Shichino, Y., Nazaret, N., Boyault, C., et al. (2012). Mmi1 RNA surveillance machinery directs RNAi complex RITS to specific meiotic genes in fission yeast. EMBO J. *31*, 2296–2308.

Hsu, P.J., Zhu, Y., Ma, H., Guo, Y., Shi, X., Liu, Y., Qi, M., Lu, Z., Shi, H., Wang, J., et al. (2017). Ythdc2 is an N^6-methyladenosine binding protein that regulates mammalian spermatogenesis. Cell Res. *27*, 1115–1127.

Huber, W., Carey, V.J., Gentleman, R., Anders, S., Carlson, M., Carvalho, B.S., Bravo, H.C., Davis, S., Gatto, L., Girke, T., et al. (2015). Orchestrating high-throughput genomic analysis with Bioconductor. Nat. Methods *12*, 115–121.

Huppertz, I., Attig, J., D'Ambrogio, A., Easton, L.E., Sibley, C.R., Sugimoto, Y., Tajnik, M., König, J., and Ule, J. (2014). iCLIP: protein-RNA interactions at nucleotide resolution. Methods *65*, 274–287.

Ivanova, I., Much, C., Di Giacomo, M., Azzi, C., Morgan, M., Moreira, P.N., Monahan, J., Carrieri, C., Enright, A.J., and O'Carroll, D. (2017). The RNA m(6)A Reader YTHDF2 Is Essential for the Post-transcriptional Regulation of the Maternal Transcriptome and Oocyte Competence. Mol. Cell *67*, 1059–1067.e4.

Jain, D., Puno, M.R., Meydan, C., Lailler, N., Mason, C.E., Lima, C.D., Anderson, K.V., and Keeney, S. (2018). *ketu* mutant mice uncover an essential meiotic function for the ancient RNA helicase YTHDC2. eLife *7*, e30919.

Jankowsky, E., and Fairman, M.E. (2007). RNA helicases–one fold for many functions. Curr. Opin. Struct. Biol. *17*, 316–324.

Jumper, J., Evans, R., Pritzel, A., Green, T., Figurnov, M., Ronneberger, O., Tunyasuvunakool, K., Bates, R., Žídek, A., Potapenko, A., et al. (2021). Highly accurate protein structure prediction with AlphaFold. Nature *596*, 583–589.

Kasowitz, S.D., Ma, J., Anderson, S.J., Leu, N.A., Xu, Y., Gregory, B.D., Schultz, R.M., and Wang, P.J. (2018). Nuclear m6A reader YTHDC1 regulates alternative polyadenylation and splicing during mouse oocyte development. PLoS Genet. *14*, e1007412.

Kim, G.-W., and Siddiqui, A. (2021). N6-methyladenosine modification of HCV RNA genome regulates cap-independent IRES-mediated translation via YTHDC2 recognition. Proc Natl Acad Sci USA *118*, e2022024118.

Krakau, S., Richard, H., and Marsico, A. (2017). PureCLIP: capturing target-specific protein-RNA interaction footprints from single-nucleotide CLIP-seq data. Genome Biol. *18*, 240.

Kretschmer, J., Rao, H., Hackert, P., Sloan, K.E., Höbartner, C., and Bohnsack, M.T. (2018). The m^{6}A reader protein YTHDC2 interacts with the small ribosomal subunit and the 5′-3′ exoribonuclease XRN1. RNA *24*, 1339–1350.

Kuleshov, M.V., Jones, M.R., Rouillard, A.D., Fernandez, N.F., Duan, Q., Wang, Z., Koplev, S., Jenkins, S.L., Jagodnik, K.M., Lachmann, A., et al. (2016). Enrichr: a comprehensive gene set enrichment analysis web server 2016 update. Nucleic Acids Res. *44* (W1), W90–W97.

Kurtenbach, S., and Harbour, J.W. (2019). SparK: a publication-quality NGS visualization tool. Preprint at bioRxiv. https://doi.org/10.1101/845529.

Lasman, L., Krupalnik, V., Viukov, S., Mor, N., Aguilera-Castrejon, A., Schneir, D., Bayerl, J., Mizrahi, O., Peles, S., Tawil, S., et al. (2020). Context-dependent functional compensation between Ythdf m^{6}A reader proteins. Genes Dev. *34*, 1373–1391.

Li, Y., Minor, N.T., Park, J.K., McKearin, D.M., and Maines, J.Z. (2009). Bam and Bgcn antagonize Nanos-dependent germ-line stem cell maintenance. Proc. Natl. Acad. Sci. USA *106*, 9304–9309.

Li, F., Zhao, D., Wu, J., and Shi, Y. (2014). Structure of the YTH domain of human YTHDF2 in complex with an m(6)A mononucleotide reveals an aromatic cage for m(6)A recognition. Cell Res. *24*, 1490–1492.

Linder, P., and Jankowsky, E. (2011). From unwinding to clamping - the DEAD box RNA helicase family. Nat. Rev. Mol. Cell Biol. *12*, 505–516.

Liu, J., Yue, Y., Han, D., Wang, X., Fu, Y., Zhang, L., Jia, G., Yu, M., Lu, Z., Deng, X., et al. (2014). A METTL3-METTL14 complex mediates mammalian nuclear RNA N6-adenosine methylation. Nat. Chem. Biol. *10*, 93–95.

Liu, J., Gao, M., Xu, S., Chen, Y., Wu, K., Liu, H., Wang, J., Yang, X., Wang, J., Liu, W., et al. (2020). YTHDF2/3 are required for somatic reprogramming through different RNA deadenylation pathways. Cell Rep. *32*, 108120.

Liu, R., Kasowitz, S.D., Homolka, D., Leu, N.A., Shaked, J.T., Ruthel, G., Jain, D., Keeney, S., Luo, M., and Pillai, R.S. (2021). YTHDC2 Is Essential for Pachytene Progression and Prevents Aberrant Microtubule-Driven Telomere Clustering in Male Meiosis. Cell Reports *37*, 110110.

Love, M.I., Huber, W., and Anders, S. (2014). Moderated estimation of fold change and dispersion for RNA-seq data with DESeq2. Genome Biol. *15*, 550.

Luecken, M.D., and Theis, F.J. (2019). Current best practices in single-cell RNA-seq analysis: a tutorial. Molecular Systems Biology *15*, e8746.

Lun, A.T., McCarthy, D.J., and Marioni, J.C. (2016). A step-by-step workflow for low-level analysis of single-cell RNA-seq data with Bioconductor. F1000Res. *5*, 2122.

Luo, S., and Tong, L. (2014). Molecular basis for the recognition of methylated adenines in RNA by the eukaryotic YTH domain. Proc. Natl. Acad. Sci. USA *111*, 13834–13839.

Mao, Y., Dong, L., Liu, X.-M., Guo, J., Ma, H., Shen, B., and Qian, S.-B. (2019). m^{6}A in mRNA coding regions promotes translation via the RNA helicase-containing YTHDC2. Nat. Commun. *10*, 5332.

Mathys, H., Basquin, J., Ozgur, S., Czarnocki-Cieciura, M., Bonneau, F., Aartse, A., Dziembowski, A., Nowotny, M., Conti, E., and Filipowicz, W. (2014). Structural and biochemical insights to the role of the CCR4-NOT complex and DDX6 ATPase in microRNA repression. Mol. Cell *54*, 751–765.

Mendel, M., Chen, K.M., Homolka, D., Gos, P., Pandey, R.R., McCarthy, A.A., and Pillai, R.S. (2018). Methylation of Structured RNA by the m(6)A Writer METTL16 Is Essential for Mouse Embryonic Development. Mol. Cell *71*, 986–1000.e11.

Mendel, M., Delaney, K., Pandey, R.R., Chen, K.-M., Wenda, J.M., Vågbø, C.B., Steiner, F.A., Homolka, D., and Pillai, R.S. (2021). Splice site m^{6}A methylation prevents binding of U2AF35 to inhibit RNA splicing. Cell *184*, 3125–3142.e25.

Meyer, K.D., Saletore, Y., Zumbo, P., Elemento, O., Mason, C.E., and Jaffrey, S.R. (2012). Comprehensive analysis of mRNA methylation reveals enrichment in 3′ UTRs and near stop codons. Cell *149*, 1635–1646.

Mosavi, L.K., Cammett, T.J., Desrosiers, D.C., and Peng, Z.Y. (2004). The ankyrin repeat as molecular architecture for protein recognition. Protein Sci. *13*, 1435–1448.

Nakagawa, T., Zhang, T., Kushi, R., Nakano, S., Endo, T., Nakagawa, M., Yanagihara, N., Zarkower, D., and Nakayama, K. (2017). Regulation of mitosis-meiosis transition by the ubiquitin ligase β-TrCP in male germ cells. Development *144*, 4137–4147.

Ohlstein, B., Lavoie, C.A., Vef, O., Gateff, E., and McKearin, D.M. (2000). The Drosophila cystoblast differentiation factor, benign gonial cell neoplasm, is related to DExH-box proteins and interacts genetically with bag-of-marbles. Genetics *155*, 1809–1819.

Özeş, A.R., Feoktistova, K., Avanzino, B.C., Baldwin, E.P., and Fraser, C.S. (2014). Real-time fluorescence assays to monitor duplex unwinding and ATPase activities of helicases. Nat. Protoc. *9*, 1645–1661.

Patil, D.P., Pickering, B.F., and Jaffrey, S.R. (2018). Reading m^{6}A in the Transcriptome: m^{6}A-Binding Proteins. Trends Cell Biol. *28*, 113–127.

Patro, R., Duggal, G., Love, M.I., Irizarry, R.A., and Kingsford, C. (2017). Salmon provides fast and bias-aware quantification of transcript expression. Nat. Methods *14*, 417–419.

Pendleton, K.E., Chen, B., Liu, K., Hunter, O.V., Xie, Y., Tu, B.P., and Conrad, N.K. (2017). The U6 snRNA m(6)A Methyltransferase METTL16 Regulates SAM Synthetase Intron Retention. Cell *169*, 824–835.e14.

Prabu, J.R., Müller, M., Thomae, A.W., Schüssler, S., Bonneau, F., Becker, P.B., and Conti, E. (2015). Structure of the RNA Helicase MLE Reveals the Molecular Mechanisms for Uridine Specificity and RNA-ATP Coupling. Mol. Cell *60*, 487–499.

Pyle, A.M. (2008). Translocation and unwinding mechanisms of RNA and DNA helicases. Annu. Rev. Biophys. *37*, 317–336.

R Core Team. (2018). R Foundation for Statistical Computing; Vienna, Austria: 2018. R: A language and environment for statistical computing. https://www.R-project.org.

Robinson, M.D., McCarthy, D.J., and Smyth, G.K. (2010). edgeR: a Bioconductor package for differential expression analysis of digital gene expression data. Bioinformatics *26*, 139–140.

Roehr, J.T., Dieterich, C., and Reinert, K. (2017). Flexbar 3.0 - SIMD and multicore parallelization. Bioinformatics *33*, 2941–2942.

Roignant, J.Y., and Soller, M. (2017). m^{6}A in mRNA: An Ancient Mechanism for Fine-Tuning Gene Expression. Trends Genet. *33*, 380–390.

Ruszkowska, A., Ruszkowski, M., Dauter, Z., and Brown, J.A. (2018). Structural insights into the RNA methyltransferase domain of METTL16. Sci. Rep. *8*, 5311.

Schwartz, S. (2016). Cracking the epitranscriptome. RNA *22*, 169–174.

Schwartz, S., Agarwala, S.D., Mumbach, M.R., Jovanovic, M., Mertins, P., Shishkin, A., Tabach, Y., Mikkelsen, T.S., Satija, R., Ruvkun, G., et al. (2013). High-resolution mapping reveals a conserved, widespread, dynamic mRNA methylation program in yeast meiosis. Cell *155*, 1409–1421.

Śledź, P., and Jinek, M. (2016). Structural insights into the molecular mechanism of the m(6)A writer complex. eLife *5*, e18434.

Smith, T., Heger, A., and Sudbery, I. (2017). UMI-tools: modeling sequencing errors in Unique Molecular Identifiers to improve quantification accuracy. Genome Res. *27*, 491–499.

Soh, Y.Q.S., Mikedis, M.M., Kojima, M., Godfrey, A.K., de Rooij, D.G., and Page, D.C. (2017). Meioc maintains an extended meiotic prophase I in mice. PLoS Genet. *13*, e1006704.

Soumillon, M., Necsulea, A., Weier, M., Brawand, D., Zhang, X., Gu, H., Barthès, P., Kokkinaki, M., Nef, S., Gnirke, A., et al. (2013). Cellular Source and Mechanisms of High Transcriptome Complexity in the Mammalian Testis. Cell Rep *3*, 2179–2190.

Stoilov, P., Rafalska, I., and Stamm, S. (2002). YTH: a new domain in nuclear proteins. Trends Biochem. Sci. *27*, 495–497.

Theler, D., Dominguez, C., Blatter, M., Boudet, J., and Allain, F.H. (2014). Solution structure of the YTH domain in complex with N6-methyladenosine RNA: a reader of methylated RNA. Nucleic Acids Res. *42*, 13911–13919.

Wang, X., Lu, Z., Gomez, A., Hon, G.C., Yue, Y., Han, D., Fu, Y., Parisien, M., Dai, Q., Jia, G., et al. (2014). N6-methyladenosine-dependent regulation of messenger RNA stability. Nature *505*, 117–120.

Wang, X., Zhao, B.S., Roundtree, I.A., Lu, Z., Han, D., Ma, H., Weng, X., Chen, K., Shi, H., and He, C. (2015). N(6)-methyladenosine Modulates Messenger RNA Translation Efficiency. Cell *161*, 1388–1399.

Wang, C., Zhu, Y., Bao, H., Jiang, Y., Xu, C., Wu, J., and Shi, Y. (2016a). A novel RNA-binding mode of the YTH domain reveals the mechanism for recognition of determinant of selective removal by Mmi1. Nucleic Acids Res. *44*, 969–982.

Wang, P., Doxtader, K.A., and Nam, Y. (2016b). Structural Basis for Cooperative Function of Mettl3 and Mettl14 Methyltransferases. Mol. Cell *63*, 306–317.

Warda, A.S., Kretschmer, J., Hackert, P., Lenz, C., Urlaub, H., Höbartner, C., Sloan, K.E., and Bohnsack, M.T. (2017). Human METTL16 is a N^6-methyladenosine (m^{6}A) methyltransferase that targets pre-mRNAs and various non-coding RNAs. EMBO Rep. *18*, 2004–2014.

Watabe, E., Togo-Ohno, M., Ishigami, Y., Wani, S., Hirota, K., Kimura-Asami, M., Hasan, S., Takei, S., Fukamizu, A., Suzuki, Y., et al. (2021). m^6 A-mediated alternative splicing coupled with nonsense-mediated mRNA decay regulates SAM synthetase homeostasis. EMBO J. *40*, e106434.

Wojtas, M.N., Pandey, R.R., Mendel, M., Homolka, D., Sachidanandam, R., and Pillai, R.S. (2017). Regulation of m6A Transcripts by the 3′→5′ RNA Helicase YTHDC2 Is Essential for a Successful Meiotic Program in the Mammalian Germline. Mol. Cell *68*, 374–387.e12.

Wu, M., Reuter, M., Lilie, H., Liu, Y., Wahle, E., and Song, H. (2005). Structural insight into poly(A) binding and catalytic mechanism of human PARN. EMBO J. *24*, 4082–4093.

Wolf, F.A., Angerer, P., and Theis, F.J. (2018). SCANPY: large-scale single-cell gene expression data analysis. Genome Biology *19*, 15.

Wu, R., Chen, Y., Liu, Y., Zhuang, L., Chen, W., Zeng, B., Liao, X., Guo, G., Wang, Y., and Wang, X. (2021). m6A methylation promotes white-to-beige fat transition by facilitating Hif1a translation. EMBO Rep. *22*, e52348.

Xiao, W., Adhikari, S., Dahal, U., Chen, Y.S., Hao, Y.J., Sun, B.F., Sun, H.Y., Li, A., Ping, X.L., Lai, W.Y., et al. (2016). Nuclear m(6)A Reader YTHDC1 Regulates mRNA Splicing. Mol. Cell *61*, 507–519.

Xu, C., Wang, X., Liu, K., Roundtree, I.A., Tempel, W., Li, Y., Lu, Z., He, C., and Min, J. (2014). Structural basis for selective binding of m6A RNA by the YTHDC1 YTH domain. Nat. Chem. Biol. *10*, 927–929.

Xu, C., Liu, K., Ahmed, H., Loppnau, P., Schapira, M., and Min, J. (2015). Structural Basis for the Discriminative Recognition of N6-Methyladenosine RNA by the Human YT521-B Homology Domain Family of Proteins. J. Biol. Chem. *290*, 24902–24913.

Yamashita, A., Shichino, Y., Tanaka, H., Hiriart, E., Touat-Todeschini, L., Vavasseur, A., Ding, D.-Q., Hiraoka, Y., Verdel, A., and Yamamoto, M. (2012). Hexanucleotide motifs mediate recruitment of the RNA elimination machinery to silent meiotic genes. Open Biol. *2*, 120014.

Yoshida, H., Park, S.-Y., Sakashita, G., Nariai, Y., Kuwasako, K., Muto, Y., Urano, T., and Obayashi, E. (2020). Elucidation of the aberrant 3′ splice site selection by cancer-associated mutations on the U2AF1. Nat. Commun. *11*, 4744.

Zaccara, S., and Jaffrey, S.R. (2020). A unified model for the function of YTHDF proteins in regulating m6A-modified mRNA. Cell *181*, 1582–1595.e18.

Zhang, Z., Theler, D., Kaminska, K.H., Hiller, M., de la Grange, P., Pudimat, R., Rafalska, I., Heinrich, B., Bujnicki, J.M., Allain, F.H., and Stamm, S. (2010). The YTH domain is a novel RNA binding domain. J. Biol. Chem. *285*, 14701–14710.

Zhu, T., Roundtree, I.A., Wang, P., Wang, X., Wang, L., Sun, C., Tian, Y., Li, J., He, C., and Xu, Y. (2014). Crystal structure of the YTH domain of YTHDF2 reveals mechanism for recognition of N6-methyladenosine. Cell Res. *24*, 1493–1496.

STAR★METHODS

KEY RESOURCES TABLE

REAGENT or RESOURCE	SOURCE	IDENTIFIER
Antibodies		
Polyclonal rabbit anti-SYCP3	Novus Biologicals	Cat. No. NB300-231, RRID:AB_1522841
Polyclonal rabbit anti-HA	Santa Cruz	Cat. No. sc-805, RRID:AB_631618
Monoclonal mouse anti-FLAG	Sigma	Cat. No. F3165, RRID: AB_259529
Anti-HA affinity matrix	Roche	Cat. No. 11815016001, RRID:AB_390914
Anti-FLAG M2 Magnetic Beads	Sigma	Cat. No. M8823, RRID:AB_2637089
Goat anti-mouse Alexa Fluor 488	ThermoFischer Scientific	Cat. No. A28175, RRID: AB_2536161
Goat anti-rabbit Alexa Fluor 594	ThermoFischer Scientific	Cat. No. A11037, RRID: AB_2534095
HRP-conjugated anti-rabbit IgG	GE Healthcare	Cat. No. NA934, RRID:AB_772206
HRP-conjugated anti-mouse IgG	Thermo Fisher	Cat. No. A27025, RRID:AB_2536089
Bacterial and virus strains		
BL21(DE3) bacterial strain	NEB	Cat. No. C2527H
DH10EMBacY bacterial strain	(Bieniossek et al., 2012)	N/A
Chemicals, peptides, and recombinant proteins		
γ-^{32}P-Adenosine triphosphate	Perkin Elmer	Cat. No. NEG002A001MC
γ-^{32}P- Adenosine triphosphate	Hartmann Analytic	Cat. No. SRP-501
40% Acrylamide/Bis Solution 19:1	Bio-Rad	Cat. No. 1610144
N,N,N',N'-Tetramethylethylendiamin	Merck	Cat. No. 1107320100
S. pyrogenes Cas9 mRNA	ThermoFischer Scientific	Cat. No. A29378
S. pyrogenes Cas9 protein	IDT	Cat. No. 1081058
S. pyrogenes Cas9 protein	PNAbio	Cat. No. CP01-20
FuGENE HD transfection reagent	Promega	Cat. No. E231A
Cre Recombinase	NEB	Cat. No. M0298
D-desthiobiotin	IBA	Cat. No. 2-1000-001
Ammonium persulphate	AppliChem	Cat. No. A2941
ATP	Thermo Scientific	Cat. No. R0441
Glycogen, RNA grade	Thermo Scientific	Cat. No. R0551
Lithium Chloride	Merck	Cat. No. 1056790250
Formic acid	Fluka	Cat. No. 06440
T4 Polynucleotide Kinase	Thermo Scientific	Cat. No. EK0031
Protease Inhibitor Tablets, EDTA-free	Thermo Scientific	Cat. No. A32965
L-Glutathione reduced	Merck	Cat. No. G4251-25G
Critical commercial assays/kits		
NEBNext® Multiplex Small RNA Library Prep Set for Illumina®	NEB	Cat. No. E7300
MinElute Gel Extraction Kit	QIAGEN	Cat. No. 28604
MEGAshortscript™ T7 Transcription Kit	Life technologies	Cat. no. AM1354
Mini elute kit	QIAGEN	Cat. No. 28004
Platinum™ II Hot-Start PCR Master Mix	ThermoFisherScientific	Cat. No. 14000012
Illustra MicroSpin G-25 micro columns,	GE Healthcare	Cat. No. 27-5325-01
Phire Green Hot Start II PCR Master Mix	Thermo Scientific	Cat. No. F126L
Deposited data		
Deep sequencing datasets	This study.	GEO: GSE196427
All raw gel data are deposited at Mendeley Data.	This study.	https://doi.org/10.17632/wrnxpfmxnd.1

(*Continued on next page*)

Continued

REAGENT or RESOURCE	SOURCE	IDENTIFIER
Experimental models: Cell lines		
Sf21 insect cells for protein production	Eukaryotic Expression Facility, EMBL Grenoble, France	N/A
High Five (Hi5) insect cells for protein production	Eukaryotic Expression Facility, EMBL Grenoble, France	N/A
Experimental models: Organisms/strains		
Mouse: *Ythdc2 knock-out*	(Wojtas et al., 2017)	EMMA: EM11456
Mouse: *Ythdc2-cat-dead*	This study.	Dominant-negative mutation, not maintained.
Mouse: *Ythdc2-YTH*	This study.	Available from Lead Contact.
Mouse: *Ythdc2-3xFLAG*	This study.	Available from Lead Contact.
Mouse: *2xHA-Meioc*	This study.	Available from Lead Contact.
Zebrafish: *ythdc2*^{D46}	This study.	Available from Lead Contact.
Oligonucleotides		
DNA and RNA oligos	N/A	See Table S1
Recombinant DNA		
pACEBac2	(Bieniossek et al., 2012)	N/A
pACEBac2S	(Wojtas et al., 2017)	Modified pACEBac2 expressing N-terminal 6xHis-Strep-SUMO-TEV fusion protein.
pACEBac2-GST	This study	Modified pACEBac2 expressing C-terminal TEV-GST fusion protein.
pIDK	(Bieniossek et al., 2012)	N/A
Software and algorithms		
FastQC v0.11.5	N/A	https://www.bioinformatics.babraham.ac.uk/projects/fastqc/
Flexbar v3.5.0	N/A	https://github.com/seqan/flexbar
SeqAn v2.4.0	N/A	https://github.com/seqan/seqan
STAR v2.7.9a	(Dobin et al., 2013)	N/A
umi_tools dedup v1.1.1	(Smith et al., 2017)	N/A
samtools merge v1.7	(Li et al., 2009)	N/A
PureCLIP v1.3.1	(Krakau et al., 2017)	N/A
SparK v2.6.2	(Kurtenbach and Harbour, 2019)	N/A
Kallisto v0.46.2	(Bray et al., 2016)	N/A
Salmon	(Patro et al., 2017)	https://combine-lab.github.io/salmon/
DESeq2	(Love et al., 2014)	N/A
seaborn package v0.10.0	N/A	https://seaborn.pydata.org/
matplotlib v3.1.3	N/A	https://matplotlib.org/
ENRICHR	(Chen et al., 2013; Kuleshov et al., 2016)	http://amp.pharm.mssm.edu/Enrichr/
Cellranger pipeline v3.0.2	N/A	https://github.com/10XGenomics/cellranger
Python v3.6.9	N/A	https://www.python.org/
Scanpy v1.4.5	(Wolf et al., 2018)	N/A
Scran bioconductor package	(Lun et al., 2016)	N/A
mnnpy package	N/A	https://pypi.org/project/mnnpy/
MAST algorithm	(Finak et al., 2015)	https://github.com/RGLab/MAST
Bioconductor	(Huber et al., 2015)	https://www.bioconductor.org/
R	(R Core Team, 2018)	https://www.r-project.org

(*Continued on next page*)

Continued

REAGENT or RESOURCE	SOURCE	IDENTIFIER
BLAST	(Altschul et al., 1997)	https://blast.ncbi.nlm.nih.gov/
edgeR	(Robinson et al., 2010)	https://bioconductor.org/packages/release/bioc/html/edgeR.html
Other		
Chelating Sepharose Fast Flow beads	GE Healthcare	Cat. No. 17-0575-01
StrepTrap HP	GE Healthcare	Cat. No. 28-9075-46
Superdex S75 10/300 GL	GE Healthcare	Cat. No. 17-5174-01
Superdex 200 10/300 GL	GE Healthcare	Cat. No. 17-5175-01
MethaPhor agarose	Lonza	Cat. No. 50180
Protino Glutathione Agarose 4B	Macherey-Nagel	Cat. No. 745500.10
TLC PEI Cellulose F	Merck	Cat. No. 1055790001
SF 900 III SFM	GIBCO	Cat. No. 12658027
Express Five SFM	GIBCO	Cat. No. 10486025
CellCarrier-96 Black, Optically Clear Bottom, Tissue Culture Treated, Sterile, 96-Well with Lid	Perkin Elmer	Cat. No. 6005550
Strep-Tactin Sepharose resin	IBA	Cat. No. 2-1201-010

RESOURCE AVAILABILITY

Lead contact

Further information and requests for resources and reagents should be directed to and will be fulfilled by the Lead Contact, Ramesh S. Pillai (ramesh.pillai@unige.ch).

Materials availability

All unique reagents including plasmids and animal models generated in this study are available from the Lead Contact without any restrictions for academic research purposes. The host institution of the Lead Contact requires the signing of a Materials Transfer Agreement (MTA) for both academic and non-academic users.

Data and code availability

Single-cell RNA-seq data and other deep sequencing data generated in the study are deposited with the Gene Expression Omnibus (GEO: GSE196427). This accession number is also provided in the key resources table. Original data including western blots, thin-layer chromatography plate scans, the raw immunofluorescence and histological microscopy images are deposited at Mendeley and are publicly available as of the date of publication. The DOI is listed in the key resources table.

This paper does not report original code. A detailed description of the use of publicly available programs is mentioned in the methods, and also listed in key resources table. Any additional information required to reanalyze the data reported in this paper is available from the Lead Contact upon request.

EXPERIMENTAL MODEL AND SUBJECT DETAILS

Animal work

Mutant mice were generated at the Transgenic Mouse Facility, University of Geneva. The mice were bred in the Animal Facility of Sciences III, University of Geneva. Mutant fish were generated and maintained in the University of Geneva zebrafish core facility.

The use of animals in research at the University of Geneva is regulated by the Animal Welfare Federal Law (LPA 2005), the Animal Welfare Ordinance (OPAn 2008) and the Animal Experimentation Ordinance (OEXA 2010). The Swiss legislation respects the Directive 2010/63/EU of the European Union. Any project involving animal work has to be approved by the Direction Générale de la Santé and the official ethic committee of the State of Geneva performing a harm-benefit analysis of the project. Animals are treated with respect based on the 3Rs principle in the animal care facility of the University of Geneva. We use the lowest number of animals needed to conduct our specific research project. Discomfort, distress, pain and injury is limited to what is indispensable and anesthesia and analgesia is provided when necessary. Daily care and maintenance are ensured by fully trained and certified staff. This research with mouse and zebrafish is licensed by the Geneva Cantonal authorities under the authorization number Pillai GE-162-19B.

Ythdc2 mutant mice

The *Ythdc2* gene is located on mouse chromosome 18 and consists of 30 exons (Figure S1A). The generation of *Ythdc2* knockout mouse line is described previously (Wojtas et al., 2017). The exon 7 encodes for parts of the N-terminal RecA domain of the RNA helicase module in YTHDC2, and specifically the ATPase motif DEVH. YTH domain is encoded in exon 27-29. We targeted the endogenous *Ythdc2* locus in mouse embryos of the hybrid background B6D2F1 (50% C57BL/6 and 50% DBA/2) with specific guide RNAs and homology repair templates to create *Ythdc2* mutant lines inactivating the RNA helicase domain and the m^6A-binding capacity of the YTH domain.

Preparation of sgRNAs. A cloning-free method (Bassett and Liu, 2014) was used to prepare DNA template for *in-vitro* synthetic single guide RNA (sgRNA) transcription. Briefly, a common reverse primer (CRISPR sgR primer) and a gene specific CRISPR forward (F) primer with T7 promoter sequence was used to PCR amplify the sgDNA template (Table S1). The following components were mixed to prepare the PCR reaction: 20 μl 5X Phusion HF buffer, 67 μl ddH2O, 2 μl 10 mM dNTPs, 5 μl, 10 μM CRISPR F primer, 5 μl 10 μM CRISPR sgR primer and 1 μl Phusion DNA polymerase. The PCR reaction was set as follows: 98°C 30 s, 35 cycles of [98°C, 10 s; 60°C, 30 s and 72°C, 15 s], 72°C 10 min, 4°C hold. PCR product (~110 bp) was agarose gel-purified using mini-elute gel extraction kit (QIAGEN; Cat. No. 28604). The purified DNA was used to produce sgRNA by *in vitro* transcription reaction using T7 promoter. *In vitro* transcription was carried out with the MEGAshortscript T7 Transcription Kit (Life technologies; Cat. No. AM1354) for 4 h at 37°C. Reactions were treated with TURBO DNase I (37°C for 15 min) to remove template DNA, phenol-chloroform extracted and precipitated with ethanol. Quality of the generated gRNAs were verified by 1% agarose gel electrophoresis.

For single-cell sequencing, we used purified 4n germ cells from P10 males of heterozygous and homozygous *Ythdc2* KO aninmals (Figure 5A). Biological duplicates were used for preparing each single-cell RNaseq library.

sgRNA generation for Ythdc2-3xFLAG-tagged mouse line

Our previous attempts to tag (3xFLAG tag with a linker) the N- and C-termini of mouse YTHDC2 resulted in homozygous knockin mice that were infertile. This suggested that tagging at these positions resulted in destabilization of the endogenous protein in mouse testes. Therefore, we chose an internal location to place the tag. Purification of the recombinant human YTHDC2 protein (Wojtas et al., 2017) revealed the presence of a minor fraction of the protein that lacked the YTH domain. Peptide mass fingerprinting revealed this to be due to proteolysis within a putative loop just before the YTH domain. Given that this internal loop is likely to be surface-accessible, we placed an in-frame 3xFLAG tag (with a linker) to create the *Ythdc2*^{FLAG} knockin mouse. Such homozygous knockin mice are fertile.

Forward (F) primer for sgRNA generation for C-terminal 3xFLAG tag in mouse YTHDC2: RRoligo868
GAAATTAATACGACTCACTATAGGCTTGGAGATCCAATAATAGTGTTTTAGAGCTAGAAATAGC

ssDNA homology oligo: RRoligo867 for insertion of 3xFLAG in exon 25 of *Ythdc2* (Strand +)
5′CCCATGTCTTCAGAAGAACTTCCTTTGGCTTCATCTTGGAGATCCAATAATAGT**ATG**GACTACAAAGACCATGACGGTGATTAT
AAAGATCATGACATCGATTACAAGGATGACGATGACAAGGGTGGAGGCGGGTCTATGAGGAAAAGTACAGCTGACACTGAGTTTG
CGGATGGATCTACTACTGGAGAAAGG 3′

We used mouse testes from P15 *Ythdc2*^{FLAG} animals for iCLIP experiments (Figure 1) and mouse testes from P20 *Ythdc2*^{FLAG}*; Meioc*^{HA} animals for anti-FLAG protein complex purifications (Figure 2).

sgRNA generation for Ythdc2^{YTH}*mutant mouse line*

Forward (F) primer for sgRNA generation for YTH domain mutation W1375A in mouse YTHDC2: RRoligo1064 (Table S1).
5′GAAATTAATACGACTCACTATAGGGTCCAGCTGACCCCCAGTCCGTTTTAGAGCTAGAAATAGC3′

Homology oligo for YTH domain mutation W1375A in mouse *Ythdc2* (strand -): RRoligo1060
5′AAATGGTGTGCAAACTGAAAGGGAAGGCTTTCTTTGCGTATCCACTCCACTTTAAATACTCCACCTAGTCCAGCTGACCC**TGCA**
TCCTGGCTCTTCTCCCTTCCTATCTCAGAAGACATCCTAGAAAATCCCTGTATAAAAATGAGGGAG 3′

Preparation of injection mix. We mixed 12.5 ng/μL of each of the gRNA with 12.5 ng/μL of a 181 nt ssDNA homology repair template (IDT), and 25 ng/μL of Cas9 mRNA (ThermoFischer Scientifique; Cat. No. A29378) in injection buffer (10 mM Tris pH 7.5, 1 mM EDTA pH 8.0). Injection mixture can be frozen at −80°C in aliquots (20 μL) prior to use.

Injection of mouse embryos of the hybrid background B6D2F1 (50% C57BL/6 and 50% DBA/2, black coat color) was carried out at the Transgenic Mouse Core Facility, University Medical Centre (CMU), University of Geneva. The NMRI (Naval Medical Research Institute) mice, which have a white coat color were used as foster mothers.

The 2n and 4n testicular germ cells from adult (P60) *Ythdc2*^{YTH} homozygous and heterozygous mice were used for RNasequencing (Figure 1M). Biological triplicates were used.

Ythdc2 E332Q mutant and Meioc^{HA} *knockin mouse line*

For these mouse knockin lines, the gRNAs were commercially synthesized [Integrated DNA Technologies (IDT)] in two parts.

Purchase and annealing of gRNA. We purchased a tracrRNA (67 bases long, IDT; Cat. No. 1072533) which is the common part of the gRNA that binds to the Cas9 protein, and a crRNA (IDT) that has complementarity of 20 bases with the genomic DNA sequence of interest plus common additional bases (GUUUUAGAGCUAUGCU) for pairing with the 3′ end of tracrRNA. The complete gRNA was obtained by annealing 200 pmol each of tracrRNA and crRNA in 1xTE buffer (1X TE buffer, pH 7.5, IDT; Cat. No. 11-05-01-05) to a final volume of 10 uL. The gRNAs mix was heated at 95°C for 5 min and then allowed to cool at room temperature for 30 min to get annealed functional gRNA. The annealed gRNA was stored at −20°C until used for injection into mouse embryos.

crRNA: /Alt1/NNNNNNNNNNNNNNNNNNNNGUUUUAGAGCUAUGCU /Alt2/

N represent the gene-specific sequence. The sequence of crRNAs used are provided below.

crRNA and ssDNA repair oligo for Meioc^{HA} mouse line

SgRNA for 2xHA tag mouse at MEIOC N-term

sgRNA1: TCCGCCGCTCACCTCCATGG

CrRNA synthesized from IDT for *Meioc* N-term targeting sgRNA1

RRoligo1142: 5′/AlTR1/rUrCrCrGrCrCrGrCrUrCrArCrCrUrCrCrArUrGrGrGrUrUrUrUrArGrArGrCrUrArUrGrCrU/AlTR2/3′

Homology ssDNA oligo for 2xHA at MEIOC N-term (reverse complement)

5′TCCCTCAGGCCTTGGGGGTGACGGGGCCGGCAGGTGTCTCCGCCGCTCACCTCCATAGACCCGCCTCCACCAGCGTAATC
TGGAACATCATATGGGTAGCCTCCACCAGCGTAATCTGGAACATCATATGGGTACATGGGGGCCCCCCAGCTCCTCCTGAGCTA
GTTAACAGCTCCCGGGGTACGGGGGTGAGGGAG 3′

crRNA and ssDNA oligo for Ythdc2$^{cat\text{-}dead}$ mouse mutant line

We made a point mutation (E332Q) within the ATP hydrolysis motif (DEVH → DQVH) present in the N-terminal RecA module of the RNA helicase domain to create the *Ythdc2$^{cat\text{-}dead}$* mice. A similar mutation (E317Q) in the recombinant human YTHDC2 inactivates the ATPase and RNA helicase activities (Wojtas et al., 2017).

sgRNA: TTCATGCACTTCATCCTGCA

CrRNA synthesized from IDT for *Ythdc2* E332Q locus targeting sgRNA

RR_crRNA_1196

5′/AlTR1/rUrUrCrArUrGrCrArCrUrUrCrArUrCrCrUrGrCrArGrUrUrUrUrArGrArGrCrUrArUrGrCrU/AlTR2/ 3′

The sequence of the ssDNA repair template for E332Q mutation is as follows:

TATTTAATTTAAACACTATAAATCCAGCAGTGTTTCCTGTTAAAGGTGAACCGTTCACAGTATTTTACCTGATCCATCATTTTGTTTC
TGTTTCTCTTCCTTGCAG**GACCAA**GTGCATGAAAG**A**GATCGATTCAGTGATTTTTTGCTTACTAAGTTAAGAGATTTGTTGCAAAAG
CACCCAACTTTG

We used mouse testes from P20 *Ythdc2^{FLAG};Meioc^{HA}* animals for anti-HA protein complex purifications (Figure 2). For *Ythdc2$^{cat\text{-}dead}$* mutant quadruplicate P14 testes were used (Figure 3).

Preparation of injection mix. Just before injection into mouse embryos, the annealed gRNAs (final concentration 0.6 pmol/μL) were mixed with the Cas9 protein at 30 ng/μL final concentration (IDT; Cat. No. 1081058) in a final volume of 9 μL. The mix was incubated at room temperature for 10 min for complex formation. For knockin mouse generation a ssDNA homology repair template (IDT; 20 ng/μL final concentration) was also added to the injection mix and volume was adjusted with 1x TE buffer, pH 7.5, to 100 μL. The injection mix was centrifuged at 13,000 rpm for five minutes at 4°C, and 50 μL of supernatant was collected and stored on ice.

Injection of mouse embryos of the hybrid background B6D2F1/J (black coat color) was carried out at the Transgenic Mouse Core Facility, University Medical Centre (CMU), University of Geneva. The NMRI (Naval Medical Research Institute) mice, which have a white coat color were used as foster mothers.

Founder mice of hybrid background B6D2F1 were identified by genotyping and crossed with wildtype C57Bl6/J (Jackson Labs) partners to obtain germline transmission. Intercrosses between heterozygous (*Ythdc2$^{KI/+}$*) knockin (KI) males and females were used to obtain homozygous (*Ythdc2$^{-KI/KI}$*) knockin males and females. Fertility was functionally assessed by crossing them with fertile heterozygous or wildtype partners. The same mutant animal was mated with a fertile partner for 1 week each, using a total of at least three different fertile partners successively. At least 3 homozygous males and females were tested. Further analyses of fertility were carried out using histological analysis of dissected ovaries and testes for comparison to the fertile control animals (Figure 1L). The heterozygous and homozygous *Ythdc2$^{cat\text{-}dead}$* founder mice of both sexes were found to be infertile when crossed with control fertile partners (Figure 3A), which prevented us from establishing the colony. All analyses with *Ythdc2$^{cat\text{-}dead}$* mutant were conducted with founder mice (Figure 3A).

Genotyping

Routine genotyping was done using ear punches of the weaned animals (which is also used for identification purposes). Ear punches were digested in 100 μl of buffer containing 10 mM NaOH, 0.1 mM EDTA for 90 min at 95°C. After centrifugation at 3000 rpm for 10 min, 50 μL of supernatant was transferred to a new tube containing 50 μl of TE buffer (20mM Tris-HCl, pH 8.0 and 0.1 mM EDTA).

For experimental mice that were euthanized before the weaning age, tail biopsies were digested in 500 μL tail buffer (50 mM Tris-HCl, pH 8.0, 100 mM EDTA, 100 mM NaCl, 1% SDS) with 2.5 μg of Proteinase K at 55°C overnight. After spinning at 16000 × g for 10 min to remove hairs, supernatants were transferred into a new tube and the DNA was precipitated by adding 500 μL of isopropanol. Samples were spun in the centrifuge at 16000 × g for 10 min, and the resulting pellet was washed with 1 mL 70% Ethanol. The pellet was dried and resuspended for at least 1 h at 37°C in 100 to 150 μL of 10 mM Tris-HCl, pH 8.0. Approximately, 1-1.5 μL of genomic DNA were used for PCR with Phire Green Hot Start II PCR Master Mix (Thermo Scientific, Cat. No. F126L).

Genotyping PCR for Ythdc2^{FLAG} mouse line

Primers RRoligo869 and RRoligo870 (Table S1) were used to amplify the edited *Ythdc2* gene locus followed by Sanger sequencing with RRoligo869 to identify the 3xFLAG-tag insertion.

Product size: 301 (KI), 214bp (WT)

PCR condition: 98°C-30 s, 35 cycles of (98°C −5 s, 60°C- 5 s, 72°C- 10 s), and 72°C −60 s.

Genotyping PCR for Ythdc2 W1375A mutant mouse line. Primers RRoligo1092 and RRoligo1093 (Table S1) were used to amplify the edited *Ythdc2* gene locus followed by sanger sequencing with RRoligo1093 to identify the *Ythdc2* W1375A mutation.

Product size: 282bp.

PCR condition: 98°C-30 s, 35 cycles of (98°C −5 s, 60°C- 5 s, 72°C- 10 s), and 72°C −60 s.

Genotyping PCR for Meioc^{HA} mouse line. Primers RRoligo1151 and RRoligo1152 (Table S1) were used to amplify the edited *Meioc* gene locus followed by sanger sequencing with RRoligo1151 to identify the *Meioc^{HA}* allele.

Product size: 282bp. 323bp (wt), 400 bp (2xHA-tagged KI allele)

PCR condition: 98°C-30 s, 35 cycles of (98°C −5 s, 63°C- 5 s, 72°C- 10 s), and 72°C −60 s. PCR reaction was supplemented with 3% DMSO.

Genotyping primer for Ythdc2$^{cat\text{-}dead}$ mutation. Primers RRoligo1358 and RRoligo1359 (Table S1) were used to amplify the edited *Ythdc2* gene locus followed by sanger sequencing with RRoligo1360 to identify the *E332Q* catalytic-dead mutation.

Product size: 600bp

PCR condition: 98°C-30 s, 35 cycles of (98°C −5 s, 60°C- 5 s, 72°C- 10 s), and 72°C −60 s.

Zebrafish Ythdc2 mutant

The *Danio rerio* (zebrafish) *ythdc2* gene is located on chromosome 5 and predicted to comprise 30 exons. To create a knockout allele of *ythdc2*, we engineered a small deletion in exon 5 of early zebrafish embryos using the CRISPR-Cas9 genome editing tool. Exon 5 encodes for part of the RNA helicase domain. Two guide RNAs were mixed with recombinant *S. pyrogenes* Cas9 protein (PNAbio; Cat. No. CP01-20) and injected into embryos of the Tubingen background. After screening multiple founders, we retained one line that germline-transmitted a 46-nucleotide deletion in *ythdc2*, resulting in removal of 123 to 456 aa from the N-terminal RecA module of the RNA helicase domain (*ythdc2$^{\Delta 46}$*). The genomic sequences for guide RNA designs, with PAM sequences in brackets, were ACGCAGCAGCGCCCCTGAGC(TGG) and TGCTCCTGGAGCTCGTAGAC(CGG).

The founder was crossed with wildtype partners to establish a colony of heterozygous *ythdc2$^{+/\Delta 46}$* animals. In-crosses between heterozygotes gave rise to *ythdc2$^{+/+}$*, *ythdc2$^{+/\Delta 46}$* and *ythdc2$^{\Delta 46/\Delta 46}$* embryos in expected Mendelian ratios. This was determined by genotyping 1 dpf embryos and 5 dpf larvae (Figure 5A). Adult homozygous *ythdc2$^{\Delta 46/\Delta 46}$* males were crossed with wildtype or heterozygous partners but did not result in any viable embryos (Figure 5B), indicating male infertility. All the homozygous mutant animals were males, and no females (based on observable phenotypes) were found.

Early embryos of the Tubingen (TU) laboratory zebrafish background were injected with approximately 1 nL per embryo of reagents for genome editing, essentially as described previously (Fish et al., 2021).

Genotyping

Zebrafish embryos, larvae or fin sections from adults were genotyped using PCR primers (Table S1) to amplify genomic DNA flanking the *ythdc2$^{\Delta 46}$* deletion site. The deletion was sufficiently large to discriminate wildtype from Δ46 alleles and assign *ythdc2$^{+/+}$*, *ythdc2$^{+/\Delta 46}$* and *ythdc2$^{\Delta 46/\Delta 46}$* genotypes based on visual examination of the products resolved in an agarose gel (Figure S5A).

METHOD DETAILS

Clones and constructs

Constructs for protein expression in insect cells

The coding sequence for full-length human YTHDC2 (1430 aa; UniProtKB - Q9H6S0) was cloned into pACEBac2S vector (modified from pACEBac2) (Bieniossek et al., 2012) to express as N-terminal 6xHis-Strep-SUMO-TEV fusion protein. The same vector was used to clone a catalytic-dead version of human YTHDC2 (hYTHDC2^{E317Q}) and YTHDC2 with ANK repeats deletion (hYTHDC2$^{\Delta ANK}$). Note we put a linker (GSAGSAAGSGEFLE) to join the two RecA domains after removal of the ANK repeats, as previously done for a mammalian expression construct (Wojtas et al., 2017). Human XRN1 truncation (1-1279 aa; UniProtKB - Q8IZH2) coding sequence was cloned into pACEBac2-GST vector (modified from pACEBac2) to express recombinant protein with C-terminal TEV-GST fusions. A catalytic-dead (E178Q) version of human XRN1(1-1279)^{E178Q} was cloned into pACEBac2-GST vector as well for use in RNA helicase assays.

To co-express full-length YTHDC2 with XRN1 (1-1279 aa), the required coding sequence for XRN1 was cloned into pIDK vector and recombined with pACEBac2S-YTHDC2 via MultiBac (Figure 2A). The coding sequence for human MEIOC coiled-coil domain (hMEIOC_CC, 740-952 aa, UniProtKB - A2RUB1) was cloned into pACEBac2-GST vector to co-express with full-length YTHDC2 protein (Figure 2B).

Since the human MEIOC_CC domain construct was not soluble when expressed alone, we expressed the mouse MEIOC coiled-coil domain (mMEIOC_CC, 721-950 aa, UniProtKB - A2AG06) as a soluble protein from the pACEBac2S vector for use in RNA helicase assays (Figure 3G, S3D, and S3G). This expressed stretch of mouse MEIOC has 91% identity with the human protein. All the clones were verified by restriction digestion of the isolated plasmids, as well as by PCR.

Baculovirus-mediated insect cell protein expression

The expression and purification of human YTHDC2 or its variants were as previously described (Wojtas et al., 2017). Similarly, for purification of individual proteins, the pACEBac2-hXRN1(1-1279)-GST or its catalytic-dead version, the pACEBac2-hMEIOC_CC-GST and pACEBac2S-mMEIOC_CC plasmids were separately transformed into DH10EMBacY competent cells for preparation of

the bacmids. The bacmid DNA was extracted and transfected with FuGENE HD (Promega; Cat. No. E231A) into the Sf9 insect cells for virus production. The supernatant (V0) containing the recombinant baculovirus was collected after 48 to 72 h post-transfection. To expand the virus pool, 2.0 mL of the V0 virus stock was added into 25 mL of Sf9 ($0.5 – 0.8 \times 10^6$/mL) cells. The resulting cell culture supernatant (V1) was collected 24 h post-proliferation arrest. For large-scale expression of the protein, Hi5 cells were infected with virus (V1) and cells were harvested 72 h after infection.

For production of YTHDC2-XRN1 complex, the pIDK-XRN1 (1-1279 aa) plasmid was recombined with pACEBac2S-YTHDC2 via Cre-recombination (NEB; Cat No. M0298S). This reaction product was transformed into DH10EMBacY competent cells for preparation of the MultiBac bacmid. The bacmid DNA was then extracted and transfected with FuGENE HD into the Sf9 insect cells for virus production. For large-scale expression of the protein, Hi5 cells were infected with virus (V1) and cells were harvested 72 h after infection.

For production of YTHDC2-hMEIOC_CC complex, Hi5 cells were co-infected with baculoviruses expressing either 6x-His-Strep-Sumo-YTHDC2 or hMEIOC_CC-GST. Cells were harvested 72 h after infection.

Purification of recombinant proteins and complexes

Purification of recombinant full-length human YTHDC2 or its variants is described (Wojtas et al., 2017).

Hi5 cells expressing XRN1 (1-1279 aa) or its catalytic mutant (E178Q) versions were resuspended by lysis buffer (50 mM Tris-HCl pH 8.0, 300 mM NaCl, 5% glycerol and 5 mM 2-mercaptoethanol) supplemented with proteinase inhibitor (Thermo Scientific, EDTA-free). Cells were disrupted by sonication and then cell lysate was centrifuged at 18,000 rpm for 50 min at 4°C. The clarified supernatant was incubated with Protino Glutathione Agarose 4B (Macherey-Nagel; Cat. No. 745500.10) at 4°C for 2 h. After incubation, beads were washed with lysis buffer and finally bound protein was eluted with 15 mM L-Glutathione reduced in lysis buffer. The C-terminal GST tag was removed by TEV cleavage overnight at 4°C during dialysis against the buffer (50 mM Tris-HCl pH 8.0, 300 mM NaCl, 5 mM 2-mercaptoethanol). After tag cleavage, protein was further purified through Superdex 200 increase 10/300 column (GE Healthcare) equilibrated with buffer (25 mM HEPES-KOH, pH 7.5, 150 mM KCl, 5% glycerol, 1 mM DTT) S2. Fractions of pure protein were confirmed by SDS-PAGE electrophoresis, flash-frozen in liquid nitrogen in 10% glycerol and stored at −80°C.

Hi5 cells expressing mouse MEIOC coiled-coil domain (mMEIOC_CC) were resuspended by lysis buffer (40 mM imidazole, 50 mM Tris-HCl pH 8.0, 300 mM NaCl, 5% glycerol and 5 mM 2-mercaptoethanol) supplemented with proteinase inhibitor (Thermo Scientific, EDTA-free). Cells were disrupted by sonication and then cell lysate was centrifuged at 18,000 rpm for 50 min at 4°C. The clarified supernatant was incubated with Ni^{2+} chelating Sepharose FF beads (GE Health; Cat. No. 17057501) at 4°C for 2 h. After incubation, beads were washed by 50/60 mM imidazole in lysis buffer and the bound protein was eluted by 250 mM imidazole in buffer (50 mM Tris-HCl pH 8.0, 300 mM NaCl, 5% glycerol and 5 mM 2-mercaptoethanol). The N-terminal 6XHis-Strep-SUMO tag was removed by TEV cleavage overnight at 4°C during dialysis against buffer (50 mM Tris-HCl pH 8.0, 300 mM NaCl, 5 mM 2-mercaptoethanol). After dialysis, the cleaved tag was removed by a second nickel column purification, and the flow-through containing untagged protein was concentrated and subjected to size-exclusion chromatography (Superdex 75 increase 10/300 column, GE Healthcare) equilibrated with buffer (25 mM Tris-HCl, pH 8.0, 150 mM KCl, 5% glycerol, 1 mM DTT). Fractions of pure protein were confirmed by SDS-PAGE electrophoresis, flash-frozen in liquid nitrogen in 10% glycerol and stored at −80°C.

Hi5 cells co-expressing YTHDC2 and XRN1 (1-1279 aa) from a MultiBac construct were resuspended in the lysis buffer (50 mM Tris-HCl pH 8.0, 300 mM NaCl, 40 mM Imidazole, 5% glycerol and 5 mM 2-mercaptoethanol) supplemented with proteinase inhibitor (Thermo Scientific, EDTA-free). Cells were disrupted by sonication and clarified by centrifugation at 18,000 rpm for 50 min at 4°C. The supernatant was incubated at 4°C for 2 h with the Ni^{2+} chelating Sepharose FF beads (GE Health; Cat. No. 17057501). After incubation, beads were washed with an imidazole gradient in the wash buffer (40 mM or 50mM imidazole, 50 mM Tris-HCl pH 8.0, 300 mM NaCl, 5% glycerol and 5 mM 2-mercaptoethanol). Proteins bound to the beads were eluted with elution buffer (50 mM Tris-HCl pH 8.0, 300 mM NaCl, 250 mM Imidazole, 5% glycerol and 5 mM 2-mercaptoethanol). Such eluate was then subjected to a second Strep column (IBA; Cat. No. 2-1201-010) purification, and finally bound protein was eluted by 5 mM desthiobiotin in buffer: 50 mM Tris-HCl pH 8.0, 300 mM NaCl, 5% glycerol and 5 mM 2-mercaptoethanol. The N-terminal 6xHis-Strep-SUMO-TEV tag was cleaved overnight with TEV in the dialysis buffer (50 mM Tris-HCl pH 8.0, 300 mM NaCl, 5 mM 2-mercaptoethanol). After dialysis, cleaved tag was removed via second nickel column and flow-through containing the untagged protein was pooled and concentrated. Concentration was done using the Pierce Protein Concentrator (Thermofisher; Cat. No. 88522). Briefly, the columns were filled up with the buffer (50 mM Tris-HCl pH 8.0, 300 mM NaCl, 5 mM 2-mercaptoethanol), spun at 4000xg, then the protein was loaded into the column and spun till the desired volume (500-600 μL) was reached. Proteins were further purified by gel filtration chromatography using Superdex 200 increase 10/300 GL (GE Healthcare) equilibrated with the buffer (25 mM HEPES-KOH pH 7.6, 150 mM KCl, 5% glycerol, 1 mM DTT). The fractions were checked by SDS-PAGE electrophoresis and the pure protein complex (Figure 2A) was flash-frozen in liquid nitrogen after addition of 10% glycerol and stored at −80°C.

To validate the direct interaction between YTHDC2 and hMEIOC_CC, Hi5 cells co-expressing 6xHis-Strep-Sumo-YTHDC2 and hMEIOC_CC-GST were resuspended in lysis buffer (50 mM Tris-HCl pH 8.0, 300 mM NaCl, 5% glycerol and 5 mM 2-mercaptoethanol) supplemented with proteinase inhibitor (Thermo Scientific, EDTA-free). Cells were disrupted by sonication and the cell lysate was centrifuged at 18,000 rpm for 50 min at 4°C. The clarified supernatant was incubated with Protino Glutathione Agarose 4B (Macherey-Nagel; Cat. No. 745500.10) at 4°C for 2 h. After incubation, beads were washed with lysis buffer and finally bound protein was eluted

by 15mM L-Glutathione reduced in lysis buffer. The glutathione eluate was checked by SDS-PAGE electrophoresis. Purification of GST-tagged hMEIOC_CC domain co-purified the 6xHis-Strep-Sumo-YTHDC2 (Figure 2B), confirming direct interactions.

YTHDC2 RNA helicase assay

The fluorescence-based helicase assay was modified from (Özeş et al., 2014).

Preparation of RNA loading strand for annealing by in vitro transcription

A 61 nt RNA was generated by *in vitro* transcription using T7 promoter. The reaction was carried out at 37°C for 4 h in a 20 μL reaction containing 6 pmol DNA template (Table S1), 2 μL 10x reaction buffer, 2 μL of 75 mM CTP/UTP/GTP/ATP and 2 μL T7 enzyme mix (MEGAshortscript T7 Transcription Kit, Cat. No. AM1354). Generated RNAs were purified by G-25 column (illustra MicroSpin G-25 micro columns, Cat. No. 27-5325-01) to remove free nucleotides, followed by phenol-chloroform extraction.

Preparation of double-stranded RNA for unwinding experiment

To prepare double-stranded RNA for the unwinding experiment, two RNAs were synthesized (Integrated DNA Technologies): a probe strand carrying 3′ Cy3 fluorophore and a quench strand carrying 5′ BHQ quencher (Figure 3E and Table S1). The annealing reaction containing 1 μL of 10 μM probe strand, 3 μL of 10 μM quench strand, 1 μL of 10 μM loading strand (prepared above), and 45 μL 1x annealing buffer (20 mM Tris-HCl pH 7.5, 100 mM KCl) was carried out at 95°C for 5 min and then slowly cooled down to 25°C in thermomixer (Eppendorf). After that, 1 μL of 100 μM DNA competitor (Table S1) was added into the reaction and incubated on ice until further use.

Fluorescence-based helicase assay

For all experiments, 160 nM protein was mixed with 20 nM annealed RNA in unwinding buffer (20 mM Tris-HCl pH 7.5, 100 mM KCl, 2 mM $MgCl_2$, 2 mM DTT) in total 100 μL reaction. The reaction mixture was loaded into 96-well plate (Perkin Elmer, Cat. No. 6005550) and the background fluorescence was measured at 37°C in Spark 10M plate reader (Tecan). The excitation wavelength was set at 540 nm and emission wavelength at 585 nm. The bandwidth for both excitation and emission was 20 nm. The background signal was measured every 15 s for 12 cycles then 100 μL of 4 mM ATP was injected into the well to induce the unwinding reaction. Change of the fluorescence intensity was recorded over time for in total 100 cycles with 30 s interval. The final concentration of protein in the reaction was 80 nM protein, 10 nM dsRNA and 2 mM ATP in unwinding buffer (20 mM Tris-HCl pH 7.5, 100 mM KCl, 2 mM $MgCl_2$, 2 mM DTT). All the measurements were set at gain 160 with Z-position at 33327 μm in SPARKCONTROL V2.1. Three individual traces for each reaction were recorded at the same time and the average of fluorescence, together with standard deviation were calculated to make the curves (Figures 3F–3H and S3C–S3H).

ATPase assay

ATP hydrolysis reactions (20 μL) contained the following components: 20 mM Tris-HCl pH 7.5, 100 mM KCl, 2 mM $MgCl_2$, 2 mM DTT and 10 μCi/mL γ-^{32}P-ATP (Hartmann Analytic; Cat. No. SRP-501). The same dsRNA (Table S1) as in the RNA helicase assay was used at final 10 nM concentration. Wildtype (WT) or catalytic-dead (E317Q) human YTHDC2 (Wojtas et al., 2017) was added at indicated concentrations (Figure 3I and S3I). When needed XRN1^{E178Q}(1-1279) was also included. Reactions were incubated at 37°C for 30 min. The reaction products were spotted on a thin layer chromatography (TLC) plate (Merck; Cat. No.1055790001), air-dried for 3-4 min, and migrated with 0.5 M LiCl, 0.5 M formic acid, in a migration chamber for 40 min. Free phosphate can be distinguished from ATP because it migrates faster during TLC. The plate was then dried at room temperature and exposed to Storage Phosphor screens (GE Health; Cat. No. 28-9564-75) and scanned with a Typhoon FLA 9500 scanner (GE Health; Cat. No. 29-1885-90). Four independent experiments were performed and quantified by ImageQuant TL. The values were normalized to YTHDC2 activity and plotted (Figure 3I). One tailed t.test was used to test whether adding XRN1^{E178Q} increases the activity above 100%.

Electrophoretic Mobility Shift Assay (EMSA)

To examine the RNA-binding property of hYTHDC2 we carried out electrophoretic mobility shift assay (EMSA) (Figure S1G). We first prepared 5′-end labeled single-stranded RNA (Table S1) and purified it by gel-elution after urea-PAGE. Synthetic RNA (20 pmol; Microsynth, CH) was 5′-end labeled with 20 μCi of γ-^{32}P-ATP (Hartmann Analytic; Cat. No. SRP-501) and 10 U of polynucleotide kinase (Thermo Scientific; Cat. No. EK0031) at 37°C for 1 h. The 20 μL reactions were cleared of unincorporated radioactive nucleotides by passing through a G25 microspin column (illustra MicroSpin G-25 micro columns, Cat. No. 27-5325-01), mixed with gel loading dye and separated by 18% urea-PAGE (1xTBE) at constant power of 18 W. The gel was briefly exposed for 10 min to Storage Phosphor screens (GE Health; Cat. No. 28-9564-75) and scanned with a Typhoon FLA 9500 scanner (GE Health; Cat. No. 29-1885-90). The band corresponding to the major radioactive species was cut out and eluted in 300 μL of 300 mM NaCl overnight by mixing (Thermomixer at 750 rpm) at 25°C. Labeled RNA was directly precipitated with 100% cold ethanol and glycogen (1 μL of 20 mg/mL stock) at −20°C for 30 min. After centrifugation, the RNA was resuspended in 20 μL of nuclease-free water.

For forming RNA-protein complexes, we incubated recombinant full-length wild-type human YTHDC2 with radioactive-labeled RNAs in 20 μL reactions containing: 20 mM Tris-HCl pH 7.5, 100 mM KCl, 2 mM $MgCl_2$ and 2 mM DTT. Proteins were used at three different concentrations: 37, 74 and 148 nM. Incubations were carried out on ice for 1 h. Reactions were mixed with 1 μL of loading dye (1x TBE, 10% glycerol, bromophenol blue and xylene cyanol) and separated out by 6% native PAGE (0.25 xTBE). Electrophoresis (running buffer was 0.25 xTBE) was carried out at 3W, 4°C for 1 h till the bromophenol blue dye is 6 cm above the end of the gel. Note that since the theoretical isoelectric point (pI) of full-length human YTHDC2 is 8.68, we adjusted pH of the gel and running buffer to

10.5. This should ensure that the proteins carry an overall negative charge under native conditions. The gel was exposed to Storage Phosphor screens and scanned with a Typhoon FLA 9500 scanner (Figure S1G).

Antibodies

Commercial antibodies

Anti-SYCP3 (Novus Biologicals; NB300-231) to detect the mouse protein. Mouse anti-HA monoclonal was a kind gift of Marc Buhler, FMI, Basel, Switzerland, while rabbit anti-HA (Santa Cruz; sc-805) and monoclonal mouse anti-FLAG (Sigma; Cat. no. F3165) were purchased. Anti-HA affinity matrix (Roche; Cat. No. 11815016001), anti-FLAG M2 Magnetic Beads (Sigma; Cat. No. M8823) were used for immunoprecipitations.

For immunofluorescence studies the following secondary antibodies coupled to fluorescent dyes were used: anti-rabbit (Alexa Fluor 594; Cat. No. A11037), anti-mouse (Alexa Fluor 488; Cat. No. A28175). For western blot analyses the following secondary antibodies conjugated to Horse Radish Peroxidase were used: anti-rabbit IgG HRP-linked (GE Healthcare; NA934), anti-mouse IgG HRP-conjugated (Thermo Fisher; Cat. No. A27025).

iCLIP

Testes from five P15 mice from *Ythdc2*^{FLAG}*; Meioc*^{HA} double homozygous knockin line (Figure 2C) were used for one experiment. The five pairs of P15 testes were digested with collagenase IV (1mg/mL in DMEM, 2ml/pair testis) at 33°C with gentle intermittent mixing in a Thermomixer (Eppendorf). After 15 min, digested testes were removed from thermomixer and gently mixed with a 1ml pipette for several times to get a single-cell suspension. The testes suspension was spun at 300xg for 5 min at 4°C. The medium was removed and the cells were collected in 10 mL cold DMEM. Cells were transferred into a 10 cm^2 Petri dish (cell culture grade) and UV cross-linked with 200mj/cm^2 (254 nm wavelength UV lamps) for 3 times on ice. After UV cross-linking, cells were collected in 15 mL falcon tubes and spun at 500xg for five minutes in at 4°C. The cell pellet was washed twice with ice-cold 1X PBS and snap-frozen in liquid nitrogen and stored at −80°C until use. The remaining procedure for iCLIP was performed as described by (Huppertz et al., 2014). RNase I digestion was done at 1:200 dilution for 3 min at 37°C with 1100 rpm mixing in a Thermomixer (Eppendorf). Anti-FLAG M2 Magnetic Beads (Sigma; Cat. No. M8823) (100μl/reaction) were used for immunoprecipitation. The final PCR amplification was performed with Platinum II Hot-Start PCR Master Mix (ThermoFisherScientific; Cat. No. 14000012) for 30 cycles. The PCR product was precipitated with sodium acetate and ethanol, separated on 3% MetaPhor agarose (Lonza; Cat. No. 50180) in 1xTAE buffer. The DNA band corresponding to 100-200 bp was cut from the gel and purified using MiniElute kit (QIAGEN; Cat. No. 28004). Purified iCLIP libraries were sequenced on NextSeq 500 illumina sequencer for 75 cycles single end. The data for the iCLIP analysis is from two biological replicates (Figure S1B).

Isolation of endogenous YTHDC2 and MEIOC complexes from mouse testes

Testes from P20 *Ythdc2*^{FLAG}*; Meioc*^{HA} double homozygous knockin line (Figure 2C) were used. We used eight testes for each experiment. Testes were lysed in 3.0ml lysis buffer (50 mM Tris-HCl pH 8.0, 150 mM NaCl, 10% glycerol, 5 mM EDTA pH 8.0, 0.5 mM DTT, 0.1% NP-40 and EDTA-free protease inhibitor from ThermoScientific) using a glass homogenizer, on ice. The lysate was cleared by centrifugation at 20000xg for first 10 min at 4°C. The supernatant was collected in a fresh tube and centrifuged again for 20 min at 20000xg 4°C. A portion (5%) of supernatant was saved as input, with the remaining supernatant being divided into two parts. One part was supplemented with 200 μl of 250 μg/mL 3xFLAG peptide (Sigma) and serves as the control. We used 100 μl per portion of anti-FLAG magnetic beads (Sigma; Cat. No. M8823), which were washed three times with 1ml lysis buffer. The lysate was then added to the washed beads and incubated at 4°C for 3 h with continuous rotation (10 rpm). After the incubation, beads were washed five times with lysis buffer (5 min for each wash at 4°C with gentle mixing). During last wash the beads were transferred to a fresh tube. The protein complexes were eluted twice with 150 μl 3xFLAG peptide (Sigma) at 37°C, 1000 rpm for 15 min in a Thermomixer (Eppendorf). The eluted complexes from two elutions were pooled. An aliquot of 20 μL from the pooled elutions was tested by PAGE and Silver staining. The experiments were performed in biological triplicates. In a separate experiment, the lysate was supplemented with RNaseA/T1 to degrade all the RNA before purifying the protein complexes (Figure 2D).

Purification of MEIOC-associated proteins was performed similarly using anti-HA affinity matrix (Roche; Cat. No. 11815016001) from testes lysate of either P20 wild type (control IP) or from P20 *Ythdc2*^{FLAG}*; Meioc*^{HA} double homozygous knockin line (Figure 2C). The lysate was supplemented with RNaseA/T1 to degrade RNA before purifying the protein complexes (Figure 2D). The MEIOC-associated proteins were eluted by boiling the beads with SDS sample loading buffer. The experiments were performed in biological triplicates.

The eluted complexes were processed at the Functional Genomics Center Zurich (ETH Zurich) using shotgun mass spectrometry analysis. Database searches were performed using the Mascot (SwissProt, mouse) search program. Applied settings: 1% protein false detection rate (FDR), min. 1 peptides per protein, 0.1% peptide FDR. To search for the proteins associated with YTHDC2-3xFLAG and 2xHA-MEIOC in mouse P20 testes, the peptide counts obtained by immunoprecipitation and mass spectrometry (IP-MS) were assigned to genes and processed using edgeR (Robinson et al., 2010). The counts were compared between the positive and control samples. For YTHDC2-3XFLAG complex purifications the control is the P20 knockin testes lysate pre-incubated with the FLAG peptide, while for 2xHA-MEIOC complex purification, the control is P20 wild-type mouse testes. The obtained log2FC values and associated adjusted p values were used to construct the volcano plots (Figure 2D). The genes with logFC > = 1 and adj. p value <= 0.05 were considered to be significantly enriched. Venn diagrams compare the enriched genes between different

immunoprecipitations (Figure S2C). The enrichment of GO Biological Process terms associated with the enriched genes was analyzed (Figure S2D) using ENRICHR.

Tissue lysates

Tissues were extracted from euthanized mice, flash-frozen in liquid nitrogen, and kept at −80°C until extract preparation. Tissues were lysed using a cell disruptor (Janke & Kunkel; IKA-WERK) in 1 mL of lysis buffer [10% glycerol, 50 mM Tris-HCl, pH8.0, 150 mM NaCl, 5 mM MgCl2, 0.5% sodium deoxycholate, 1% Triton X-100, complete protease inhibitor cocktail (Roche; Cat. No. 5056489001)]. After disruption, SDS was added to a final of 2% and gently sonicated for 10 s to breakdown genomic DNA. Aliquots were frozen in −80°C and separated by 8% SDS-PAGE, transferred to a nitrocellulose membrane and probed with antibodies.

Western Blot

Whole cell lysates were separated on SDS-PAGE gels in order to detect proteins of interest. In short, SDS-PAGE gels were prepared using Ultra-Pure ProtoGel 30% acrylamide (37.5:1) (National Diagnostic; Cat. No. EC-890) mixed with ultra-pure water and resolving gel buffer to obtain 8% resolving gel (0.375 M Tris, 0.1% SDS, pH 8.8), and with stacking gel buffer to obtain 8% stacking gel (0.125 M Tris, 0.1% SDS, pH 6.8). N,N,N',N'-Tetramethylethylendiamin (Merck; Cat. No. 1107320100) and 10% ammonium persulfate were added to catalyze the polymerization reaction. Gel electrophoresis was performed at 90 V for 30 min. and then at 120 V for 90 min. After separation, proteins were blotted on the Amersham Protran 0.45 μm nitrocellulose membrane (GE Healthcare; Cat. No. 10600002) overnight at 5 V at room temperature using Trans-Blot SD. Semi-Dry Transfer Cell system (Bio-Rad; Cat. No. 1703940). After transfer, membranes were washed with Tris-buffered saline (TBS, 20 mM Tris, 150 mM NaCl, pH 7.6) and blocked for 1 h at room temperature with 5% dry milk in TBS with 0.05% Tween20 (TTBS) (Sigma; Cat. No. P7949). After 1 h, membranes were incubated with primary antibody for 1 h at RT in 5% milk with TTBS. Then, membranes were washed 5 times for 5 min with TTBS and incubated with HRP-conjugated secondary antibody at 1:10 000 dilution, with either anti-rabbit IgG HRP-linked (GE Healthcare; Cat. No. NA934) or HRP-conjugated anti-mouse IgG (ThermoFischer; Cat. No. A27025) for 1 h at RT in 5% milk in TTBS. After 1 h, membranes were washed 5 times for 5 min with TTBS followed by 3 washes for 5 min with TBS and incubated with one of the detection reagents: Amersham Prime Western Blotting Detection Reagent (GE Healthcare; Cat. No. RPN2232), SuperSignal West Femto Maximum Sensitivity Substrate (ThermoFisher; Cat. No. 34095) or Pierce ECL 2 Substrate (ThermoFisher; Cat. No. 1896433A) for 5 min. at room temperature. Signal was detected using Amersham Hyperfilm ECL (GE Healthcare; Cat. No. 28906837). The processed films were scanned using Perfection 3200 Photo scanner (Epson) with XSane image scanning software (ver. 0999).

Histology and Immunofluorescence

Histology of mouse tissue sections

To prepare the paraffin sections, isolated testes or ovaries were fixed in Bouin's solution (Sigma; Cat. No. HT10132) overnight at room temperature. Samples were transferred into the embedding cassettes (Simport; Cat. No. M508-3) and subsequently washed for 1 h in tap water and then transferred to 1x PBS. Specimens were sent to the histology platform (CMU, University of Geneva) where they were dehydrated in 70% (2 × 2 h), 90% (1 h), 95% (1 h) and 100% ethanol (3 × 30 min) followed by incubation in HistoSAV-xylolersatz (3 times 30 min; Biosystems). The solution was removed and replaced with paraffin, and incubated at 56-58°C. Testes were then transferred into plastic molds (Polysciences mold S-22; Cat. No. NC0397999) filled with paraffin, and paraffin was allowed to solidify at room temperature. The sections (~5 μm thickness) were cut using microtome (Leica RM2135) and mounted on the Superfrost Plus microscope slides (Thermo Fisher; Cat. No. 4951PLUS4). The sections were allowed to stretch for 24 h at 42°C and then were stored at room temperature.

For histological analysis, the slides containing the paraffin sections were placed in a glass slide holder filled with HistoSAV (3 × 5 min) to remove the paraffin. For rehydration, the slides were incubated in 3x 100% ethanol, 96% ethanol, 70% ethanol, 50% ethanol and water (3 min for each step). Sections were stained with Hematoxylin solution (Merck) for 3-5 min and rinsed in running tap water. Then, sections were stained with Eosin Y solution (Sigma Aldrich; Cat. No. E4382) for 3 to 5 min and washed with water. For dehydration, the sections were incubated in 50% (30 s), 70% (30 s), 96% (30 s), 100% ethanol (2 min) and HistoSAV (3 × 3 min). Few drops of Neo-Mount (Merck) were deposited on the sections and immediately covered with coverslips. Pictures were taken using microscope AXIO Imager M2 (Zeiss).

Immunofluorescence of mouse tissue sections

Collected testes were washed in PBS and immediately fixed in 10 mL of 2% paraformaldehyde at 4°C for 3 h on a rotating wheel. Tissues were washed twice in 1x PBS and dehydrated in 15% sucrose in 1x PBS for almost 3 h (till the testes/ovaries sink to the bottom of the falcon tube). After a further dehydration step in 30% sucrose overnight, tissues were embedded in a cryomold (Tissue-Tek) filled with Andwin Scientific Tissue-Tek CRYO-OCT Compound (Fisher Scientific; Cat. No. 14-373-65) and frozen on dry ice. Embedded tissues were cut at histology platform (CMU, University of Geneva) using cryostat (Leica CM3050). The 7 μm tissue sections were mounted on Superfrost Plus glass slides and stored at −80°C. For immunofluorescence experiments, sections were allowed to dry at room temperature for 30 min and fixed in cold 4% paraformaldehyde in PBS (on ice) for 10 min. Slides were then washed in PBS at RT (2 × 5 min), and once in distilled water (5 min). Next, antigen retrieval was performed with Heat-Induced Epitope Retrieval (HIER). Briefly, slides were submerged in 600 mL of 10 mM Citrate Buffer pH 6.0 (2.1 g citric acid, 1.0 g NaOH pellet dissolved in 1000 mL MiliQ water) and heated in a microwave at full power (600 W) for 20 min. Tissues were allowed to cool down at room

temperature for at least 45 min, washed in PBS and permeabilized in 0.3% Triton X-100 in PBS at RT for 10 min. Slides were washed twice in TBS-T (TBS; 20 mM Tris, 150 mM NaCL, pH 7.6, and 0.1% Tween20) and blocked for minimum 30 min at room temperature in a humidified chamber in blocking buffer (5% normal goat serum in TBS-T). Primary antibodies were diluted in blocking buffer at different concentrations (see below) and incubated overnight at 4°C. Next day, slides were washed twice in TBS-T, incubated with secondary antibody diluted in blocking buffer (anti-mouse or anti-rabbit conjugated to Alexa 488, or 594 fluorophore) in a humidified chamber for 45-60 min (dilution 1:1000). Slides were washed twice in TBS-T and incubated with DAPI (0.5 μg/mL, Bio-Rad; Cat. No. 10043282) for 5-15 min to counterstain the nuclei. Sections were finally washed twice in TBS-T, once in ddH_2O and mounted with Slowfade Gold Antifade Reagent (Life technologies; Cat. No. S36942). Pictures were taken using Zeiss LSM780 confocal microsocope (Bioimaging Center, University of Geneva).

Primary antibodies concentrations: anti-SCP3 1:200 (Novus Biologicals; NB300-231).

Histology of zebrafish tissue sections

6-month-old adult male zebrafish were euthanized and fixed whole in 4% formal/PBS for 3 days at 4°C. Samples were mounted into histology cassettes and rinsed with water prior to dehydration, paraffin embedding and sectioning. Sections were mounted onto microscope slides and stained with hematoxylin/eosin. The latter steps were performed by the University of Geneva, faculty of medicine histology platform. Samples were imaged using a Zeiss AxioCam instrument.

FACS purification of mouse germ cells for RNaseq and single-cell RNA sequencing

Male pups (P10) or adult (P60) mice were euthanized for testes collection. Testes were removed and placed in a Petri dish (3 cm) with PBS and transferred in another Petri dish containing 1.5 mL DMEM supplemented with 1mg/mL type IV collagenase (Sigma; Cat. No. C5138). All extraneous tissue and the tunica are removed, and the seminiferous tubules teased apart. The samples are transferred into a 2ml Eppendorf and put at 35°C in a water bath for 15 min. The tubes were regularly inverted for mixing. After centrifugation for 5 min at 278x g (1610 rpm in Mikro22R) testes are resuspended in pre-warmed 500 μL 0.125% Trypsin and incubated for 6 min at 35°C. The Tryptic digest was stopped by addition of DMEM with 10% FBS. The solution is mixed gently into a suspension by pipetting at least 10 times. Centrifuge for 5 min. at 200xg (1360 rpm in Mikro22R). Resuspend the cells with 1ml or more of FACS buffer (1x PBS with 1% BSA). Filter with a 100 μm cup Filcon (BD; Cat. No. 340639). Check the viability with trypan blue (stains only dead cells), count and dilute in FACS buffer at about 4x106 cell/mL. Put on ice and move to FACS instrument.

We used Hoechst or Drak5 to stain DNA just before sorting (9 μL of Drak5 for 3.9x106 cell/mL) to isolate 1n, 2n and 4n cells. The 2n and 4n testicular germ cells from adult (P60) *Ythdc2*^{YTH} homozygous and heterozygous mice were used for RNasequencing (Figure 1M). Biological triplicates were used.

For single-cell sequencing, we used purified 4n germ cells from P10 males of heterozygous and homozygous *Ythdc2* KO aninmals (Figure 5A). Biological duplicates were used.

For *Ythdc2*$^{cat\text{-}dead}$ mutant quadruplicate P14 testes were used.

Preparation of RNA libraries

Sequencing of testicular RNA

Total RNA was isolated using the Trizol reagent (ThermoFisher Scientific; Cat. No. 15596026) from the required mouse testes samples (whole testes or FACS purified germ cells). RNA concentration was measured with a Qubit fluorimeter (Life Technologies) and RNA integrity assessed with a Bioanalyzer (Agilent Technologies). The TruSeq Stranded Total RNA kit with Ribo-Zero Gold was used for library preparation with 500 ng of total RNA as input. Library molarity and quality was assessed with the Qubit and Tapestation using a DNA High sensitivity chip (Agilent Technologies). Libraries were diluted at 2 nM and pooled before the clustering process on a HiSeq 4000 Single Read flow cell. Reads of 50 bases were generated using the TruSeq SBS reagents on the Illumina HiSeq 4000 sequencer (iGE3 Genomics Platform, University of Geneva).

Single cell sequencing

Mouse testes from *Ythdc2* heterozygous (HET) and homozygous *Ythdc2* KO P10 mice (Wojtas et al., 2017) were collected and single-cell suspensions prepared for FACS purification of 4n germ cells, as described above. We pooled cells from two individual mice of the same genotype together to obtain sufficient number of cells. The cells were captured on the 10x Genomics Chromium system. The Chromium Single Cell 3′ Reagent Kit version 2 kit was used for library preparation according to manufacturer's specifications. Library molarity and quality was assessed with the Qubit and Tapestation and loaded on a Paired-end 100 flow cell. Thus, each dataset consists of cells from two P10 mice (four pairs of testes). For *Ythdc2* HET we used one dataset, while for *Ythdc2* KO two datasets were used.

QUANTIFICATION AND STATISTICAL ANALYSIS

iCLIP

Two replicate YTHDC2 iCLIP datasets from P15 mice were used in this analysis (Figure S1B). The analysis strategy was mainly based on the previously published approach (Busch et al., 2020). Quality of the library was checked with FastQC v0.11.5 and adapters were removed with Flexbar v3.5.0 and SeqAn v2.4.0 (Roehr et al., 2017). Trimmed reads were aligned to the mouse genome reference (GRCm38) by STAR v2.7.9a (Dobin et al., 2013) with the following iCLIP-specific parameters:–outFilterMismatchNoverReadLmax

0.04–outFilterMismatchNmax 999–outFilterMultimapNmax 1–alignEndsType Extend5pOfRead1. Generated BAM files were deduplicated with umi_tools dedup v1.1.1 (Smith et al., 2017). The BAM files were merged together with samtools merge v1.7 (Li et al., 2009) and PureCLIP v1.3.1 (Krakau et al., 2017) was used to identify binding sites from the merged BAM file. The binding sites BED file generated by the PureCLIP algorithm was further annotated by intersecting binding site coordinates with the gene coordinates obtained from the GRCm38 genome annotation file (Ensembl release 102) by using bedtools intersect. Pie charts (Figure 1B) were produced with matplotlib pie function by intersecting binding sites genomic coordinates with either 5′UTR/CDS/3′UTR/intron genomic coordinates, or with gene coordinates with the regard to gene biotype. *Cul4a* gene coverage track (Figure 1B) was plotted using SparK v2.6.2 (Kurtenbach and Harbour, 2019). Heatmap of z-scores (Figure 1C) and metaplot (Figure 1D) of the average binned coverage across all genes encoding YTHDC2-bound transcripts (transcript with the highest number of exons was considered as the canonical isoform) were produced based on the average coverage per bin of the binned transcript areas (5′ UTR = 50 bins, CDS = 200 bins, 3′ UTR = 100 bins) with either matplotlib bar or seaborn clustermap functions, respectively. Total number of annotated binding sites was taken to produce scatterplots (Figures 1E and 1F) with the matplotlib scatter function. Binding site coordinates were extended to 5-mers and their sequences were taken from the GRCm38 genome reference file (Ensembl release 102) both for 3′ UTR- and CDS-specific sites, and their frequencies were compared (Figure 1F). Total number of 5-mer sequences was overlapped, and position-specific nucleotide frequencies were computed to make a sequence logo with logomaker python package. Highly confident binding sites were retained based on the binding site coverage criteria ($0 < \log2(\text{BS coverage}) < 4.5$) to plot the histogram of the total number of binding sites per YTHDC2 binding target (Figure 1G). GO term analysis of the highly confident YTHDC2 binding targets was performed with ENRICHR (Chen et al., 2013; Kuleshov et al., 2016) (Figure 1H). Total number of binding sites was taken to perform the comparative analysis of the UUUU-stretch frequencies versus DRACH motif frequencies (Figure 1J). Motif frequencies (Figures 1J, S1E, and S1F) were computed by using sliding window approach with the window size of 5 and step = 1 in case of non-match, otherwise step = 5 (motif length). Frequencies were normalized per total number of motifs identified at a certain position.

Analysis of RNA-seq data

Quality control of the demultiplexed libraries was performed with FastQC. Sequencing adapters were removed with Flexbar software. For the analysis of the catalytic dead mutant (Figures 3A and S3B), reads were aligned to the mouse transcriptome (GRCm38 assembly) with kallisto quant RNA-seq quantification tool v0.46.2 (Bray et al., 2016). All the other RNA-seq datasets were aligned to the transcriptome reference using salmon quant v1.3.0 (Patro et al., 2017). Transcript counts were collapsed into gene counts and DESeq function of the DESeq2 bioconductor package (Huber et al., 2015; Love et al., 2014) was used to obtain shrunken log2 fold changes of gene expression between control and mutant samples, and the adjusted p values. Adjusted p value 0.05, as well as the absolute value of log2 fold change 1.5 were defined as thresholds of statistical significance. All the visualizations were done in Python 3.6.9. Volcano plot of differential gene expression in the *Ythdc2*^{YTH} mutant was plotted using scatterplot function of the seaborn package (v0.10.0) with additional matplotlib (v3.1.3) customizations (Figure 3A). Heatmap of the differentially expressed genes in different stages of spermatogenesis was plotted with clustermap function with z_score and weighted hierarchical clustering options of the seaborn package (Figure 3B). Genes found to be significantly up- or downregulated in the mutant were searched for enriched Gene Ontology terms in the Biological Process ontology using ENRICHR (Chen et al., 2013; Kuleshov et al., 2016) and plotted (Figure S3B). RNA sequencing data from different purified spermatogenic populations- Spermatogonia, spermatocytes, spermatids, and spermatozoa (Figure 3B)- were obtained from (Soumillon et al., 2013), and processed according to the aforementioned procedure.

Analysis of single cell sequencing data

The whole single-cell RNaseq (scRNA-seq) analysis strategy was based on a previously published approach Luecken and Theis, 2019. Demultiplexed raw sequencing data were processed by cellranger pipeline (v3.0.2) developed by 10x Genomics. Reads were aligned to the custom mm10 mouse genome reference by cellranger count. Cell count matrix, gene and barcode tables were taken as final output for further processing. Scanpy scRNA-seq toolkit v1.4.5 was mainly used to integrate, normalize, and process the data. Once integrated, scRNA-seq dataset was filtered based on the following criteria: 1) transcript counts per cell (cells containing less than 1500 or more than 40000 transcripts were discarded) using filter_cells function; 2) genes expressed per cell (cells with less than 2000 genes expressed were discarded) using filter_cells function; 3) mitochondrial gene fraction (cells with more that 20% of mt genes per total number of genes expressed were discarded); 4) gene occurrence (genes which were found in less than 20 cells were discarded) with filter_genes function. Finally, 4528 cells were retained for further analysis (1151 cells of *Ythdc2*$^{+/-}$ and 3377of *Ythdc2*$^{-/-}$ genotypes). Scran bioconductor package (Lun et al., 2016) was used for the normalization with default parameters on count matrices before constructing single-cell maps. To reduce the dimensionality of the data and construct single-cell maps UMAP algorithm was applied to the normalized count matrices based on 3000 highly variable genes identified (Figure 4). Batch correction was done by MNN algorithm with mnnpy package. Leiden clustering algorithm (leiden function of the scanpy package) was used to identify cell populations with further cluster annotation based on scRNA-seq atlas of the spermatogenesis (Ernst et al., 2019). MAST algorithm was used to perform differential gene expression analysis (diffxpy.api python package). We gratefully acknowledge the extensive use of R (R Core Team, 2018) and BLAST (Altschul et al., 1997) in this study.